공학박사 학위논문

Investigation of medium-range order in amorphous GeTe and $Ge_2Sb_2Te_5$ using density functional theory and neural network potential

밀도범함수 이론 및 인공신경망 퍼텐셜을 사용한 비정질 GeTe 및 $Ge_2Sb_2Te_5$의 중거리 차수 연구

2020년 8월

서울대학교 대학원
재료공학부
이 동 헌

공학박사 학위논문

Investigation of medium-range order in amorphous GeTe and $Ge_2Sb_2Te_5$ using density functional theory and neural network potential

밀도범함수 이론 및 인공신경망 퍼텐셜을 사용한 비정질 GeTe 및 $Ge_2Sb_2Te_5$의 중거리 차수 연구

2020년 8월

서울대학교 대학원
재료공학부
이 동 헌

Investigation of medium-range order in amorphous GeTe and $Ge_2Sb_2Te_5$ using density functional theory and neural network potential

밀도범함수 이론 및 인공신경망 퍼텐셜을 사용한 비정질 GeTe 및 $Ge_2Sb_2Te_5$의 중거리 차수 연구

지도교수 한 승 우

이 논문을 공학박사 학위논문으로 제출함

2020년 8월

서울대학교 대학원

재료공학부

이 동 헌

이동헌의 공학박사 학위 논문을 인준함

2020년 8월

위 원 장: _____
부위원장: _____
위 원: _____
위 원: _____
위 원: _____

Abstract

Phase change memory (PCM) is a promising non-volatile memory. Among emerging memories, PCM has been successfully commercialized and mature technology. However, there is still a lack of understanding of the phase transition process at the atomic scale. Since molecular dynamics simulation can provide insight into crystallization kinetics of phase change materials, we perform the crystallization simulations and show that the medium-range orders in amorphous phase change materials are critical in crystallization kinetics.

We develop neural network potentials (NNP) for GeTe as a representative phase change material and investigate the crystallization process of amorphous GeTe. With the accuracy of density functional theory (DFT) level and much cheaper computational cost, we achieve the realistic simulations using the NNP. In developing the NNP, we find that overly flattened fourfold rings in the amorphous structure exaggerate the crystallization process, especially for nucleation. By explicitly including relaxation paths from flat to puckered fourfold rings, we obtain a modified NNP, which produces medium-range orders that are more consistent with DFT. This structural change increases interfacial energy between crystalline and amorphous phases and suppresses the nucleation. Using the modified NNP, we perform crystallization simulations at two densities (equilibrium density and crystalline density) and temperatures ranging from 500 to 650 K. We observe finite incubation times at both densities. In particular, the incubation time at the equilibrium density is found to be 7 or 17 ns, which is consistent with experiments.

In practice, properties of the phase change materials are tuned by doping and Ge-Sb-Te alloys are mainly used. However, developing NNP for the multi-component systems is challenging at the present, we study the effects of Al and Ga dopants using *ab initio* calculations. We find that the two dopants behave similarly in amorphous

$Ge_2Sb_2Te_5$ (GST), and they are mostly coordinated by Te atoms in a tetrahedral geometry, which is similar to those in crystalline M_xTe_y (M=Al or Ga). The number of wrong bonds increases as dopant atoms predominantly bond with Te atoms, which affects the medium-range order structures. The number of fourfold ring structures, especially ABAB-type, decreases significantly and the number of odd-numbered rings is increased, explaining the enhanced thermal stability and slow crystallization speed of doped amorphous GST in the experiment.

keywords: Phase change materials, Density functional theory, Neural network potential, Molecular dynamics, Crystallization

student number: 2014-21434

Contents

List of Tables

List of Figures

Chapter 1

Introduction

1.1 Phase change memory

In the present computational systems, memories like dynamic random access memory (DRAM), static random access memory (SRAM), and NAND flash memory are generally used. In a central process unit (CPU), the volatile memory is used for immediately accessible data with high speed, while the non-volatile memory (NVM) stores information for long-term persistent usage. Due to poor capacity in the volatile memory, data should be transferred from NVM with a large capacity. This process mainly limits the overall performance of the system. Also, demands on memory and storage grow faster and faster. Many types of emerging memory technologies have been intensively investigated to break the limit and satisfy the demands. They are summarized in Fig. 1.1. While most of the emerging memories are still immature, phase change memory (PCM) is commercialized recently using 3D XPoint developed by Intel and Micron Technology. It is expected that PCM bridges the gap between memory like DRAM and flash storage.

PCM makes use of the fast and reversible phase transition between crystalline and amorphous phases. [1] The popular phase change materials are based on Ge-Sb-Te alloys known for large contrast in optical and electrical properties between crystalline

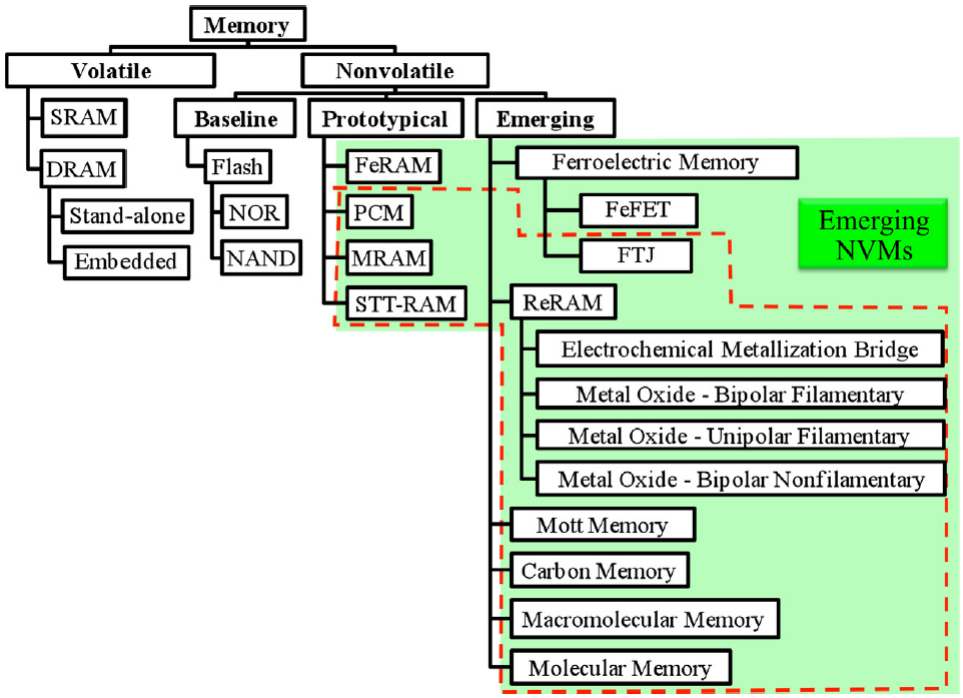

Fig. 1.1: Memory technology taxonomy. (The figure comes from the reference [4].)

and amorphous states. [2, 3] The crystalline state shows low resistance and large reflectivity, which is ON state, while the amorphous state shows high resistance and low reflectivity representing OFF state. A typical PCM cell structure is known as mushroom cell and the schematic operation flow of PCM is shown in Fig. 1.2. The SET operation of recrystallization is achieved with low voltage (current) of pulse, and the RESET operation of amorphization is achieved with high voltage (current) of the pulse.

$Ge_2Sb_2Te_5$ lying on the GeTe-Sb_2Te_3 pseudo-binary tie line benefits from rapid phase-switching ($\sim$100 ns), low power consumption, high thermal stability (10-yr retention time at room temperature), and long cyclability ($\sim 10^8$). In spite of outstanding performance, further improvements are needed in specifications like data retention, power consumption, and switching speed to compete with the current memory type on the market. For comparison, some features are tabulated in Table 1.1.

In terms of switching speed, writing speed (SET operation) is a bottleneck since it is much slower than erasing speed (RESET operation). If a writing speed can be reduced to sub-10 nanoseconds, it can directly compete with conventional memories such as DRAM. During the writing operation, the crystallization kinetics of the phase change materials has been a subject of intensive studies in both experiment and theory. In experiments, important properties of the materials such as viscosity, the activation energy for crystallization, glass transition temperature, crystallization temperature have been measured. Effects of doping or pre-treatments on crystallization have been investigated. However, it is too short to directly capture the phase transition due to the switching time of the nanoseconds scale.

On the theoretical side, crystallization simulations using *ab initio* molecular dynamics (AIMD) based on the density functional theory (DFT) can deepen understanding of crystallization kinetics at the atomic scale. For example, Hegedüs and Elliott found that crystallization of GST starts from clustered fourfold rings. [5] Furthermore, AIMD simulations can show the effects of dopants. Bi dopants shorten the crystallization time since its octahedral geometry makes fourfold rings clustered. [6] On the

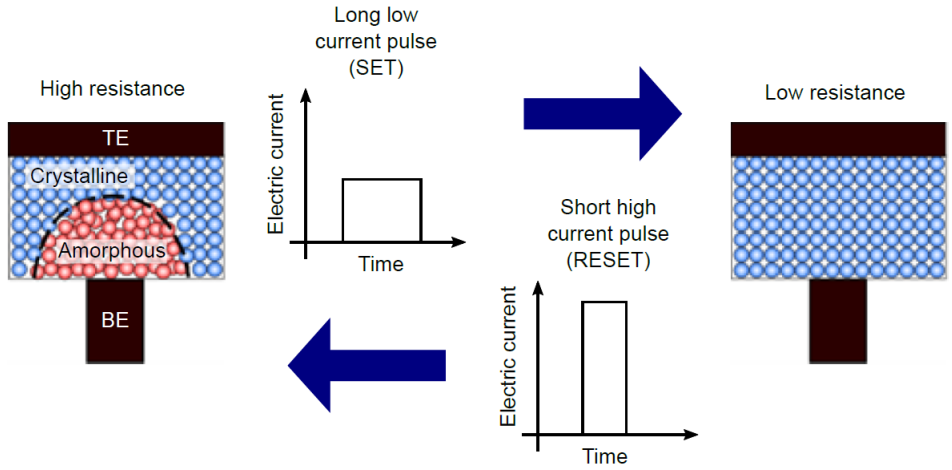

Fig. 1.2: A schematic operation principle of the mushroom-type cell of phase change memory. (The figure comes from the reference [8].)

Table 1.1: Comparison of DRAM, PCM, and NAND Flash

Features	DRAM	PCM	NAND Flash
Type	volatile	non-volatile	non-volatile
Erase time	10 ns	10-100 ns	50 μs
Write time	10 ns	100-500 ns	500 μs
Endurance	10^{15}	$10^6 - 10^8$	$10^4 - 10^5$

other hand, N dopants hinder the growth of crystal planes by distorting planar four-fold rings. [7] However, since AIMD is limited to model systems with a few hundreds of atoms, the computational results on disordered phases are significantly influenced by finite-size effects. Recently, machine learning potential (MLP) like a neural network potential (NNP) and Gaussian approximation potential (GAP) is attracting much attention as a breakthrough to overcome the limitations of *ab initio* calculations.

1.2 Goal of the dissertation

The main purpose of the dissertation is to reveal the relation between crystallization kinetics and structural features of amorphous phase change material using *ab initio* calculations and neural network potential. First, we develop neural network potentials for the crystallization of amorphous GeTe. NNP enables modeling the simulation to scale up close to the realistic device. While the accuracy and reliability of the neural network potential are refined, we find that medium-range order structural features in amorphous GeTe have crucial effects on crystallization. In addition, the relation between the medium-range order structures and crystallization kinetics is analyzed within classical nucleation theory. Second, we generate the amorphous models of Al- and Ga-doped $Ge_2Sb_2Te_5$, and structural properties are characterized within the DFT framework. Unlike the medium-range order of the pristine amorphous GeTe, Al- and Ga doping increases the homopolar bonds like Ge-Ge, Ge-Sb, and Sb-Sb and make the odd-numbered rings more. We investigate the effects of these structural changes on the crystallization of GST. Through the study, we present the relation between the medium-range order structural features in the amorphous state and the crystallization of phase change materials.

1.3 Organization of the dissertation

The dissertation is organized into five chapters. Chapter 1 is an introduction, which gives an overview of phase change memory as well as the goal of the dissertation. Chapter 2 introduces the theoretical backgrounds on the related subjects, such as density functional theory, neural network potential, and classical nucleation theory. The main results are divided into two chapters. Chapter 3 addresses the neural network potentials for GeTe. We treat the issue of the previous literature and show that the medium-range order is important for crystallization kinetics. Chapter 4 discusses the structural properties of Al- and Ga-doped amorphous $Ge_2Sb_2Te_5$. Structural properties are characterized and compared to undoped amorphous $Ge_2Sb_2Te_5$. Finally, we summarize and conclude the dissertation in Chapter 5.

Chapter 2

Theoretical background

2.1 Molecular dynamics

2.1.1 Classical molecular dynamics

Molecular dynamics (MD) is a computational technique to simulate the motion of atoms. The time evolution of positions and momenta of atoms are followed by Newton's equation of motion expressed by

$$\mathbf{r}(t+\Delta t) = \mathbf{r}(t) + \mathbf{v}(t)\Delta t + \frac{1}{2}\mathbf{a}(t)\Delta t^2 \tag{2.1}$$

where $\mathbf{r}(t)$, $\mathbf{v}(t)$, and $\mathbf{a}(t)$ represent the atomic coordinates, the velocities, and the accelerations at time t, respectively. Once the initial conditions and the interatomic potential are specified, trajectories of atoms or molecules are determined by integrating the equation. Verlet algorithm is one of the efficient integration methods and followed by

$$\mathbf{r}(t+\Delta t) = 2\mathbf{r}(t) - \mathbf{r}(t-\Delta t) + \mathbf{a}(t)\Delta t^2. \tag{2.2}$$

The atomic position of next time step $(t+\Delta t)$ is calculated from Eq (2.2). [9] Here, the time step Δt should be determined carefully for accurate and efficient MD simulations. As the time step is too large, the motions of atoms with high-frequency modes are

poorly described. On the other hand, as the time step is too small, the computational time is needed excessively.

Force calculation

In the above equations, the acceleration $\mathbf{a}(t)$ at time t is obtained from atomic forces by Newton's second law. If a mathematical expression of potential energy is analytically known, the atomic forces can be obtained from derivatives of the potential energy. In classical molecular dynamics using an interatomic potential, the potential energy of the interatomic potential is defined in terms of the atomic coordinates and fitted by a set of parameters to describe the given system accurately. Hence, the reliability of the MD simulations is depending on the quality of the interatomic potential. In addition, a choice of the interatomic potential determines the viable size of the system and simulation times because there is a trade-off between accuracy and computational cost.

Thermostat

During MD simulation the temperature of the system is related to the average kinetic energy. The relation is followed by

$$\langle E_{kin} \rangle = \frac{3}{2} N k_B T. \tag{2.3}$$

In the canonical ensemble (NVT) where the particle number N, the volume V, and the temperature T are fixed, the temperature is controlled in various ways like the Nosé-Hoover thermostat, the Berendsen thermostat, and the Langevin dynamics, and the velocity scaling. Among them, the Nosé-Hoover thermostat is one of the widely used thermostat and employed in this dissertation. A Hamiltonian of the system is written

by Eq. (2.4) where an extra degree of freedom s is introduced for heat bath. [10, 11]

$$H = \sum_{i=1}^{N} \frac{p_i^2}{2m_i s^2} + U(r) + \frac{p_s}{2Q} + g k_B T \ln s \tag{2.4}$$

$$\frac{dp_s}{dt} = \frac{1}{s}\left(\sum_{i}^{N} \frac{p_i^2}{m_i s^2} - g k_B T \right)$$

where U(r) is the potential energy of the system, Q is an imaginary mass representing the correlation between the system and the heat bath, and g is the number degrees of freedom of the extended system, $(3N + 1)$. Using this thermostat, the temperature of the system is controlled to the target temperature.

2.1.2 *Ab initio* molecular dynamics (AIMD)

AIMD is a computation method based on quantum mechanics. In principle, interacting of electrons and nuclei in materials is described by Schrödinger equation. The many-body Hamiltonian is written as

$$\begin{aligned}\hat{H} = &-\frac{\hbar^2}{2m_e}\sum_i \nabla_i^2 + \sum_{i,I}\frac{Z_I e^2}{|\overrightarrow{R_I} - \overrightarrow{r_i}|} + \frac{1}{2}\sum_{i\neq j}\frac{e^2}{|\overrightarrow{r_i} - \overrightarrow{r_j}|} \\ &-\sum_I \frac{\hbar^2}{2M_I}\nabla_I^2 + \frac{1}{2}\sum_{I\neq J}\frac{Z_I Z_J e^2}{|\overrightarrow{R_I} - \overrightarrow{R_J}|}\end{aligned} \tag{2.5}$$

where $\overrightarrow{R_I}$ indicates the position of the I^{th} nucleus and $\overrightarrow{r_i}$ indicates the position of the i^{th} electron. Z_I and M_I indicate charge and mass of the I^{th} nucleus. The first and the fourth terms are the kinetic energy of electrons and nuclei, respectively. The other three terms represent electron-nucleus, electron-electron, and nucleus-nucleus interactions in order.

The Born–Oppenheimer approximation

In general, nuclei move very slowly than electrons since nuclear mass is much larger than the electron mass. Assuming the mass of the nuclei is infinity, we can neglect the kinetic energy of the nuclei. That is, positions of the nuclei are fixed and the fourth term in Eq. (2.5) can be removed. This enables us to treat the motion of the nuclei and the electrons separately, which is called Born–Oppenheimer approximation. [12] Then, Eq. (2.5) can be reduced to

$$\begin{aligned}\hat{H} &= -\frac{\hbar^2}{2m_e}\sum_i \nabla_i^2 + \frac{1}{2}\sum_{I\neq J}\frac{Z_I Z_J e^2}{|\overrightarrow{R_I} - \overrightarrow{R_J}|} + \sum_{i,I}\frac{Z_I e^2}{|\overrightarrow{R_I} - \overrightarrow{r_i}|} + \frac{1}{2}\sum_{i\neq j}\frac{e^2}{|\overrightarrow{r_i} - \overrightarrow{r_j}|} \\ &= \hat{T}_e + \hat{E}_{II} + \hat{V}_{ext} + \hat{V}_{int}\end{aligned} \tag{2.6}$$

where $\hat{T}_e$ is the kinetic energy operator of electrons, $\hat{E}_{II}$ is the classical interaction energy between nuclei, $\hat{V}_{ext}$ is the external potential acting on electrons due to nuclei, and $\hat{V}_{int}$ is the potential interaction among electrons. As the problem of interacting of

electrons and nuclei is reduced to the problem of interacting of electrons in a static potential, it is still infeasible to solve the above many-body Hamiltonian for any practical systems.

The Hohenberg-Kohn theorems

As an approach to solving Eq. (2.6), density functional theory (DFT) has been widely used. For a N-particle system, $3N$ degrees of freedom in the equation can be reduced to 3 spatial coordinates by employing a particle density $n(\vec{r})$. DFT is based on two theorems developed by Hohenburg and Kohn. [13] The theorems are followed as:

- **Theorem I:** For any many-body system in an external potential $V_{ext}(\vec{r})$, a particle density in the ground state $n_0(\vec{r})$ determines the unique potential $V_{ext}(\vec{r})$ except a constant.

- **Theorem II:** With a universal functional for the energy $E[n(\vec{r})]$ and any external potential $V_{ext}(\vec{r})$, the energy of the system reaches the ground state at the global minimum of this functional where the particle density is the ground state.

Since the Hamiltonian of Eq. (2.6) is uniquely determined by the particle density in the ground state $n_0(\vec{r})$, the wavefunctions of all states are given by solving the Schrödinger equation. It follows from the theorem II that the ground state particle density $n_0(\vec{r})$ can be obtained by minimizing the energy functional $E[n(\vec{r})]$ corresponding to the total energy of the system expressed by

$$E[n(\vec{r})] = T[n(\vec{r})] + E_{II} + \int n(\vec{r}) V_{ext}(\vec{r}) d\vec{r} + E_{int}[n(\vec{r})]. \tag{2.7}$$

The Kohn-Sham ansatz

The Hohenberg and Kohn theorems simplified the many-body Hamiltonian, but it is still unsolvable because of the demanding degrees of freedom resulting from electron-electron interaction. Kohn and Sham suggested replacing the complex interacting many-body system with a different auxiliary non-interacting system and assumed that the

ground state particle density of the original system should be equal to that of the non-interacting system. Then, the Hamiltonian of the system is rewritten as

$$\hat{H}_{KS} = -\frac{\hbar^2}{2m_e}\sum_i \nabla_i^2 + \sum_i V_{eff}(\overrightarrow{r_i}). \tag{2.8}$$

The electron density $n(\vec{r})$ is a sum of squared modulus of wavefunctions of non-interacting electrons

$$n(\vec{r}) = \sum_i |\psi_i(\vec{r})|^2, \tag{2.9}$$

and the kinetic energy of the electrons is

$$T_s = -\frac{\hbar^2}{2m_e}\sum_i \langle\psi_i|\nabla_i^2|\psi_i\rangle. \tag{2.10}$$

The effective potential $V_{eff}(\overrightarrow{r_i})$ is introduced to take into consideration all interacting many-body effects and is defined as a sum of the external potential $V_{ext}(\overrightarrow{r_i})$, Hartree energy $V_{Hartree}(\overrightarrow{r_i})$, and exchange-correlation potential $V_{xc}(\overrightarrow{r_i})$. Using V_{eff}, the Schrödinger equation becomes a one-electron problem by the variational principle as

$$\left[-\frac{h^2}{2m}\nabla_i^2 + V_{\mathit{eff}}\rho(\overrightarrow{r})\right]\phi_i(\overrightarrow{r}) = \epsilon_i\phi_i(\overrightarrow{r}). \tag{2.11}$$

Finally, the many-body problem is simplified as the single-particle problem which is called the Kohn-Sham equation. The single-particle problem of Eq. (2.11) can be solved by the self-consistent method. In the method, the initial electron density is guessed from atomic charge densities and used to solve the Eq. (2.11). New electron density is computed and compared with the initial electron density. If the difference between the two electron densities is larger than a given criterion, the computed electron density is used to solve the Eq. (2.11). This iterative process is repeated until the difference is smaller than the criteria.

Exchange-correlation energy

It is noteworthy that the exact functional form of the exchange-correlation energy is unknown. Since the exchange-correlation part V_{xc} of the effective potential originates

from quantum mechanical effects of interacting electrons in the system, some approximations are developed to solve the Kohn-Sham equation. Among them, two approximations are widely used in solid-state systems. One is local density approximation (LDA) which is first introduced by Kohn and Sham in 1965. [14] It is assumed that the exchange-correlation energy of the system is regarded as that of the homogeneous electron gas. The exchange-correlation energy at r is the same as that of the electron-gas system with uniform charge density ρ.

$$E_{xc}^{LDA}[\rho(r)] = \int \epsilon_{xc}^{LDA}(\rho(r))\rho(r)dr \tag{2.12}$$

The other is generalized gradient approximation (GGA) first developed by Perdew and Becke. [15, 16] In principle, GGA is similar to LDA except that it contains the inhomogeneity of electron density considering the gradient of electron density.

$$E_{xc}^{GGA}[\rho(r)] = \int \epsilon_{xc}^{GGA}(\rho(r), |\nabla\rho(r)|)\rho(r)dr \tag{2.13}$$

In this dissertation, GGA is used for exchange-correlation energy parameterized by Perdew, Becke, and Ernzerhof (PBE). [17, 18] It is because GGA improves the description of the binding energy of molecules and the cohesive energy of solids with respect to LDA. [19]

Force calculation

Unlike classical interatomic potentials, the atomic forces can be obtained without any parameters in DFT. The forces are given via Hellmann-Feynman theorem

$$F_i = \nabla E_0(\overrightarrow{r}) = \frac{\partial}{\partial \overrightarrow{r}}\langle\psi_0|\hat{H}(\overrightarrow{r})|\psi_0\rangle \tag{2.14}$$

where E_0 and ψ_0 are the ground state energy and the ground state wavefunction, respectively. According to the Born–Oppenheimer approximation and the Hohenberg-Kohn theorems, all structures during AIMD simulations have unique electron density in the ground state. Therefore, accurate atomic forces are obtained within a DFT framework.

2.2 Neural network potential

Unlike other classical interatomic potentials, a neural network potential (NNP) has no constraints for physics- or chemistry-based function forms and acts as just a mathematical function that has a large number of parameters (weights). This makes NNP work in complex chemical environments like phase transition or bonds breaking/forming without prior knowledge.

2.2.1 Neural network model

A neural network is a mathematical model, which is inspired by the network of neurons in the brain. A schematic neural network model is shown in Fig. 2.1. The neural network consists of nodes and the connection lines between the nodes. In each node, a computed value is assigned as the weighted sum of the previous layer, which is expressed by

$$x_i^{l+1} = f_a(b_i^l + \sum_{j=1}^{N^l} x_i^l w_{ij}^l) \tag{2.15}$$

where x_l^i is the value of i^{th} node in l^{th} layer, N^l is the number of nodes in l^{th} layer, w_{ij}^l is the weight connecting x_j^l and x_i^{l+1} , and b_i^l is a bias which controls the offset. The activation function f_a gives non-linearity to the model in order to enhance the flexibility of the neural network. In general, a sigmoid function $f_a(x) = 1/(1 + e^x)$ is used as the activation function. This calculation is performed from an input layer to an output layer, which is called as a feed-forward neural network.

Based on the simple neural network model, a high-dimensional NNP for atomistic simulations is proposed by Behler and Parrinello. [20] The high-dimensional NNP is an assembly of atomic neural networks assigned to each atom type as shown in Fig. (2.2). For the high-dimensional NNP to predict total energy and atomic forces, The total energy is computed by a sum of atomic energies and expressed by

$$E_{total} = \sum_{i=1}^{N} E_{at}(G_i) \tag{2.16}$$

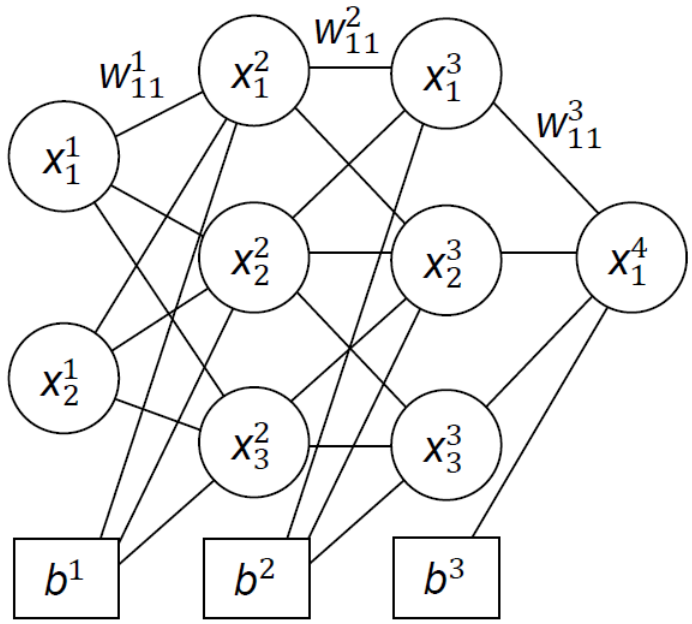

Fig. 2.1: Schematic diagram of feedforward neural network with two hidden layers.

where G_i means the symmetry function vector of i^{th} atom which will be discussed later. The atomic forces are calculated by differentiating the total energy with respect to the atomic coordinates and followed by

$$F_{i,\alpha} = -\frac{\partial E_{total}}{\partial R_{i,\alpha}} = -\sum_{j=1}^{N}\sum_{d=1}^{D_G}\frac{\partial E_{at,j}}{\partial G_{j,d}}\frac{\partial G_{j,d}}{\partial R_{i,\alpha}} \tag{2.17}$$

where $R_{i,\alpha}$ is the $\alpha(= x, y, z)$ coordinate of atom i, $G_{j,d}$ is a d^{th} component of symmetry function of atom j, and D_G is the dimension of symmetry function vector. The atomic energy of i^{th} atom is evaluated from the atomic neural network where the same atomic species share the same atomic neural network. The input of the atomic neural network is a descriptor of the local chemical environment for each atom and should have a fixed dimension to be employed regardless of the system size. The Cartesian coordinates of atoms are encoded into the symmetry function vectors describing the local environments. In this approach, the high-dimensional NNP can be employed to a large-scale system with the same network model after trained with small systems.

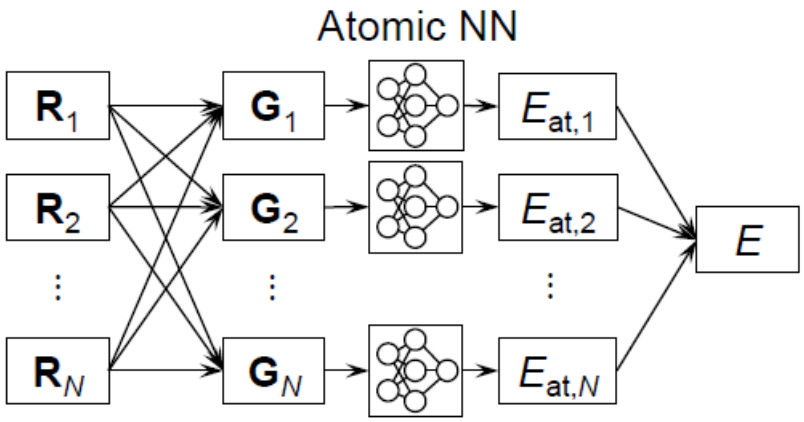

Fig. 2.2: Schematic diagram of high-dimensional neural network.

2.2.2 Atom-centered symmetry function

In the early version of the NNP, the neural network is used with the Cartesian coordinates or interatomic distances as input vectors. However, there are some limitations to extend various applications. One thing is that the network should be trained for every a given size of the system since the number of atoms in the system determines the dimension of the input vector. Another thing is that demanding computing power is required for large-scale systems. The other thing is that since the symmetry invariance of translation or rotation is not involved, the NNP can result in different energy for symmetrically identical structures. In order to overcome the limitations, Behler and Parrinello suggested the high-dimensional NNP which can be applied to the arbitrary size of systems and the symmetry function vector as the input vector to take the symmetry invariance into consideration. [20]

The atom-centered symmetry function is used for the input vector of the high-dimensional NNP. The atom-centered symmetry function describes the relation between a center atom and neighboring atoms within a cutoff radius in terms of interatomic distances and angles. The atom-centered symmetry functions are usually composed of one radial type of functions and two types of angular functions. They are defined as

$$G_i^{radial} = \sum_j e^{-\eta(R_s - R_{ij})^2} \cdot f_c(R_{ij}) \tag{2.18}$$

$$f_c(R_{ij}) = \begin{cases} \frac{1}{2}\cos\left(\frac{R_{ij}}{R_c}\pi\right) + \frac{1}{2} & (R_{ij} \leq R_c) \\ 0 & (R_{ij} > R_c) \end{cases}$$

$$G_i^{angular,1} = 2^{1-\zeta} \sum_{j,k\neq j} (1+\lambda\cos(\theta_{ijk}))^{\zeta} e^{-\eta(R_{ik})^2+R_{ij})^2+R_{jk})^2} \cdot f_c(R_{ij}) \cdot f_c(R_{ik}) \cdot f_c(R_{jk}) \tag{2.19}$$

$$G_i^{angular,2} = 2^{1-\zeta} \sum_{j,k\neq j} (1+\lambda\cos(\theta_{ijk}))^{\zeta} e^{-\eta R_{ij})^2+R_{ik})^2} \cdot f_c(R_{ij}) \cdot f_c(R_{ik}) \tag{2.20}$$

where i is the index of the center atom and j and k are those for neighboring atoms, and R_{ij} , R_{ik}, and R_{jk} are distances between them. In Eq. (2.19), and R_s determine

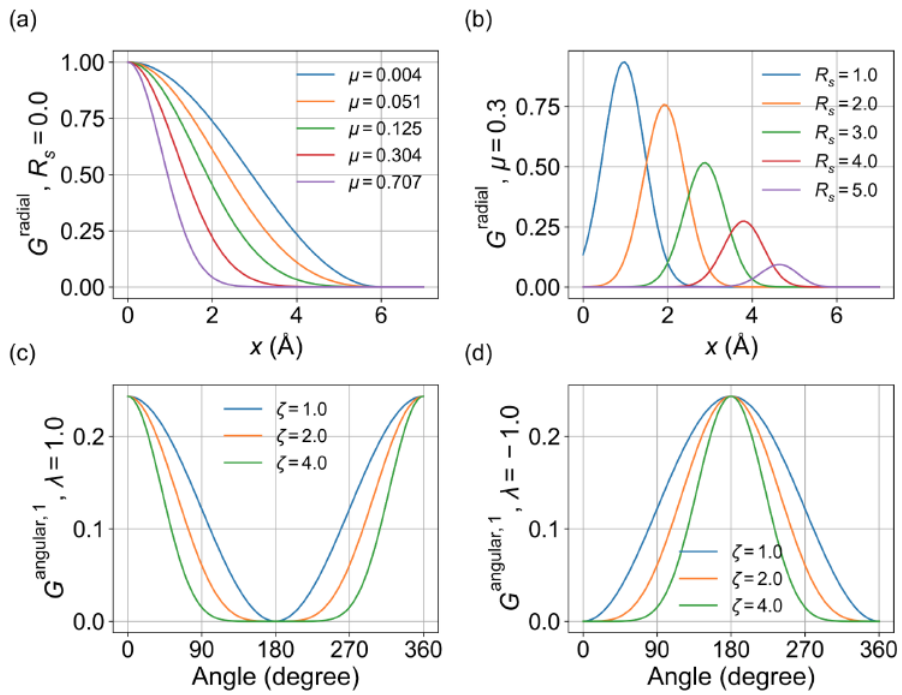

Fig. 2.3: The shape of the symmetry function according to the coefficients. For the G^{radial} function, the shape of the function according to (a) μ and (b) R_s is presented and for the $G^{angular,1}$ function, the shape of the function according to ζ is presented with the (c) $\lambda = 1$ and (d) $\lambda = -1$

the width and center of Gaussian functions, respectively, while and in Eqs. (2.19) and (2.20) changes the shape of angular functions. The cutoff function $f_c(R_{ij})$ smoothly decreases to zero as R_{ij} approaches R_c and the local environment depends on atoms within R_c. A vector G with a set of symmetry functions with various coefficients describes the local environment around the i^{th} atom. The schematic curves of the symmetry functions with the coefficients are plotted in Fig. 2.3 (a)-(d).

In principle, information loss for local environments is inevitable in representing Cartesian coordinates in the real space using the atom-centered symmetry function space. For better description of local environments, it helps to increase the number of the atom-centered symmetry functions. In addition, the set of parameters of the atom-centered symmetry functions should also be chosen. If the number of the atom-centered symmetry functions are too small, they cannot resolve different local environments, resulting in low predicting power. On the other hand, when many parameters are applied for the atom-centered symmetry functions, the computational cost of training and execution as well as the accuracy of the NNP is increased. Therefore, a set of parameters is carefully chosen to describe the local environment with sufficient resolution. It should be balanced between the accuracy and the computational cost at the same time.

For the multi-component system, the number of pairs and triplets in the symmetry functions are increased quadratically. For example, in the binary system consisting of A and B, pairs for the radial symmetry function are A-A, B-B, and A-B. Triplets (around A) for the angular symmetry function are A-A-A, A-A-B, and B-A-B triplets. It is not necessary to share the same parameter set with symmetry functions, but typically, the number of radial symmetry functions is increased with the number of elements and the number of angular symmetry functions is increased with square of the number of elements. Since the computational cost of the NNP depends on the number of symmetry functions and is proportional to the square of the number of elements, the multi-component systems is challenging to balance between the accuracy and the

computational cost. In addition to the original forms suggested by Behler, [20] some variants like weighted atom-centered symmetry function (wACSF) [21] and ANI-1 version [22] were suggested to alleviate this computational cost. Here, they are out of the scope of this dissertation and not discussed in detail.

2.2.3 Training method

Preprocessing

Before training, preprocessing the input vector helps to train the neural network model efficiently. Here, two preprocessing methods are employed to improve the training speed of the neural network model and the accuracy and stability of NNP.

In general, the values of the symmetry function have no limit and can vary with a wide range depending on the local environments. For example, one may have small values when some kinds of bonds are bare. The others may have large values when some kinds of bonds are sufficient. Since the weight corresponding to the large-value symmetry function should be changed more significantly than that corresponding to the small-value one during training, the neural network model can be biased due to the large component. Therefore, it is crucial to scale each symmetry function vector to a similar range.

There are various ways to scale the symmetry functions. One simple method is to linearly scale values of symmetry function with the range of $[-1, 1]$. Another method is that all the means of symmetry functions are set to zero and the values of the symmetry function are scaled by standard deviations. Such linear scaling methods are easy to be implemented and effective to reduce bias effects of the large-value symmetry function.

In addition to scaling, the atom-centered symmetry function has another issue that they are highly correlated to one other. The neural network is basically capable of recognizing distinct features in the correlated inputs, but it requires more training time and higher error convergence. Therefore, it is helpful to decorrelate input features in the preprocessing step to improve training speed and accuracy. One of the effective ways to decorrelating the input vectors is employing principal component analysis (PCA) which linearly transforms variables into decorrelated variables.

With the data matrix X (dimension of $N \times D_G$), the covariance matrix of X can

be computed and diagonalized as followed by

$$\Sigma = cov(X) = X^T X = U \Lambda U^T \tag{2.21}$$

where U and Λ are the eigenvector matrix and diagonal matrix of Σ, respectively. Then, the transformed data matrix Z can be defined whose covariance matrix is diagonal as given by

$$Z = U^T X. \tag{2.22}$$

Since the eigenvectors of Σ are orthogonal, the transformed data in Z is decorrelated.

Depending on the training data, the variances of each principal component can vary. Since such behavior is bad for training, each principal component is scaled to have the same variance, which is called whitening. In principle, the whitening is performed by dividing each principal component by its standard deviation. It is noteworthy that adding a small constant to the variance helps to prevent the principal components with too small variances from being scaled up. Then, the transformed data with whitening is expressed by

$$z_i^{whiten} = \frac{z_i}{\sqrt{\text{Var}(z_i) + \epsilon}} \tag{2.23}$$

where ϵ is the small and positive value used as a limit of scaling. The distributions of the transformed data by scaling, PCA, and whitening are plotted in Fig. 2.4 (b)-(d). In this dissertation, all the symmetry functions are linearly scaled into [-1,1] and the preprocess of PCA and whitening is performed in the preprocessing step.

Optimization

The target of the neural network model is to predict the accurate potential energy of the system and atomic forces. During the training, the weights in the neural network model are updated by minimizing a loss function. The iterative update of the weights gradually gives accurately predicted values compared to the reference values. In the

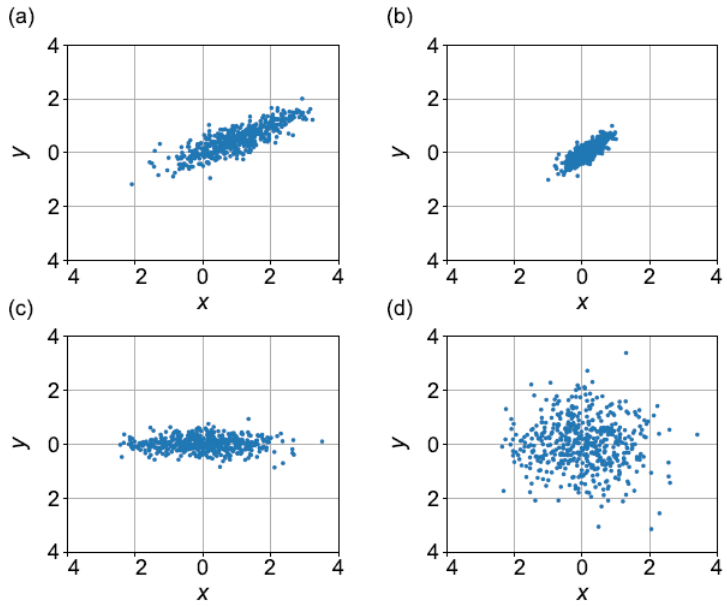

Fig. 2.4: The two-dimensional examples for input value scaling. (a) is the original distribution of the dataset and (b) is the scaled data with the range of [-1, 1].With PCA, the distribution of the dataset is converted into (c) and (d) is the whitened distribution of (c).

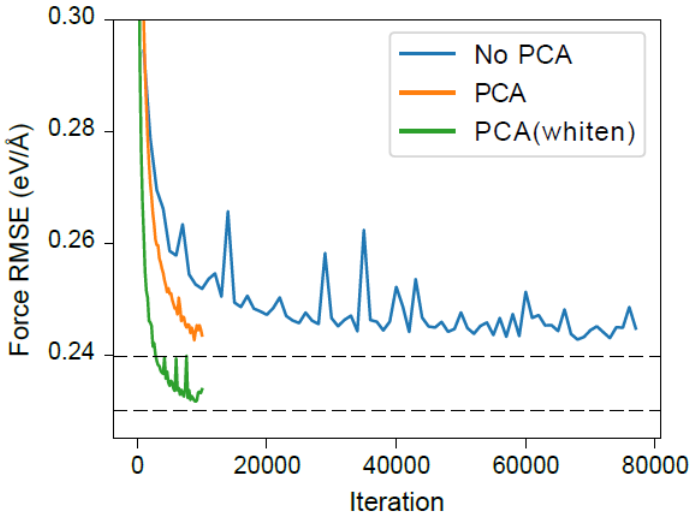

Fig. 2.5: Convergence of validation force RMSE against the training iteration with and without PCA and whitening. The blue line indicates the results without PCA preprocessing, and the orange line is the results with PCA preprocessing, but no whitening. The green line shows the results when both PCA and whitening are applied. The horizontal dashed lines indicate the converged RMSE value without PCA and with PCA and whitening. The training set consists of molecular dynamics trajectories of liquids and crystals in GeTe system.

optimization, it is important to define an appropriate functional form of the loss function. Here, the loss functions for energy, force, and stress are defined as followed.

$$\Gamma_E = \frac{1}{M}\sum_{i=1}^{M}(\frac{E_i^{DFT} - E_i^{NNP}}{N_i})^2 \tag{2.24}$$

$$\Gamma_F = \frac{1}{3\sum_{i=1}^{M} N_i}\sum_{i=1}^{M}\sum_{j=1}^{N_i}|F_{ij}^{DFT} - F_{ij}^{NNP}|^2 \tag{2.25}$$

$$\Gamma_S = \frac{1}{6M}\sum_{i=1}^{M}|S_i^{DFT} - S_i^{NNP}|^2 \tag{2.26}$$

where M is the total number of structures in the training set, and N_i is the number of atoms in an i^{th} structure. E_i, F_{ij}, and S_i are the energy of the i^{th} structure, the force of a j^{th} atom in the i^{th} structure, and the virial stress of the i^{th} structure, respectively. The total loss function is simply defined as a sum of three kinds of loss functions with the coefficients (α, β, and γ) to balance the order of magnitude among energy, force, and stress.

$$\Gamma = \alpha\Gamma_E + \beta\Gamma_F + \gamma\Gamma_S \tag{2.27}$$

The coefficients α, β, and γ can be adjusted so that the three loss functions contribute similarly to the optimization process. For specific training (only energy or weighted force training), one can adjust the coefficients.

Before the optimization process, the weight should be initialized carefully since using the activation function like sigmoid is vulnerable to gradient vanishing. If the weights are too large, the derivative of the activation function will be close to zero and the weight update will be negligible. Therefore, it is recommended that the weights are randomly initialized with a normal or uniform distribution. Xavier or He methods are simple ways to initialize the weights with a normal distribution. In Xavier initialization, the weights are randomly generated along with the normal distribution of a zero mean and a standard deviation of $\sqrt{2/(n_{in} + n_{out})}$ where n_{in} and n_{out} are the number of the nodes in the previous layer and in the next layer, respectively. In He

initialization, the weights are randomly generated along with the normal distribution of a zero mean and a standard deviation of $\sqrt{2/(n_{in})}$.

Regularization

As the training is going on, the neural network model predicts more accurate energies and forces for the structures corresponding to the training set. Figure 2.6 shows the fit quality of the neural network model with training. If the size of the neural network model is too small or training is not enough, the neural network model cannot predict the target function with the training set, which is called underfitting. After proper training, the model is trained with the training points and predicts the energy function between the training points. However, when overtrained, the model is too limited to the training set and poor at predicting the energy function between the training points. This is called overfitting.

Since the overtrained model should be inappropriate for MD simulations, overfitting must be prevented. In general, overfitting is handled in two ways. One is that the neural network model is simplified by reducing the number of input data or the size of the model, and the other is that a regularization scheme is applied during training. The former strategy has the potential to degrade the accuracy of the NNP and there are no clear criteria to determine the architecture of the model. Here, the regularization method is used to prevent overfitting.

Regularization methods such as weight decay and dropout can prevent overfitting effectively. The weight decay, or L2 regularization, is implemented by adding a penalty term in terms of the L2 norm of the weights to the loss function, which is followed by

$$\Gamma_{L2} = \lambda \|w\|_2^2. \tag{2.28}$$

This works since the L2 norm of the weights has to be large for overfitting. Therefore, the penalty term is decreased with the overall weights decreased as the training proceeds. However, a regularization constant λ should be carefully determined. If it is too

large, the model will behave like an undertrained model. On the other hand, if it is too small, the regularization effect will not work.

Dropout [23] also prevents overfitting. By randomly ignoring some nodes and weights during training, the weights are stochastically updated. It can be regarded as an efficient method to average out models.

In the early stopping method, a validation set should be prepared which is different from the training set. Usually, the data set is divided into a training set and a validation set. The errors of the training set and validation set are monitored during training. When the validation error is larger than the training error, it is considered that the overfitting occurs. Then, training should be stopped early just before the validation error is larger.

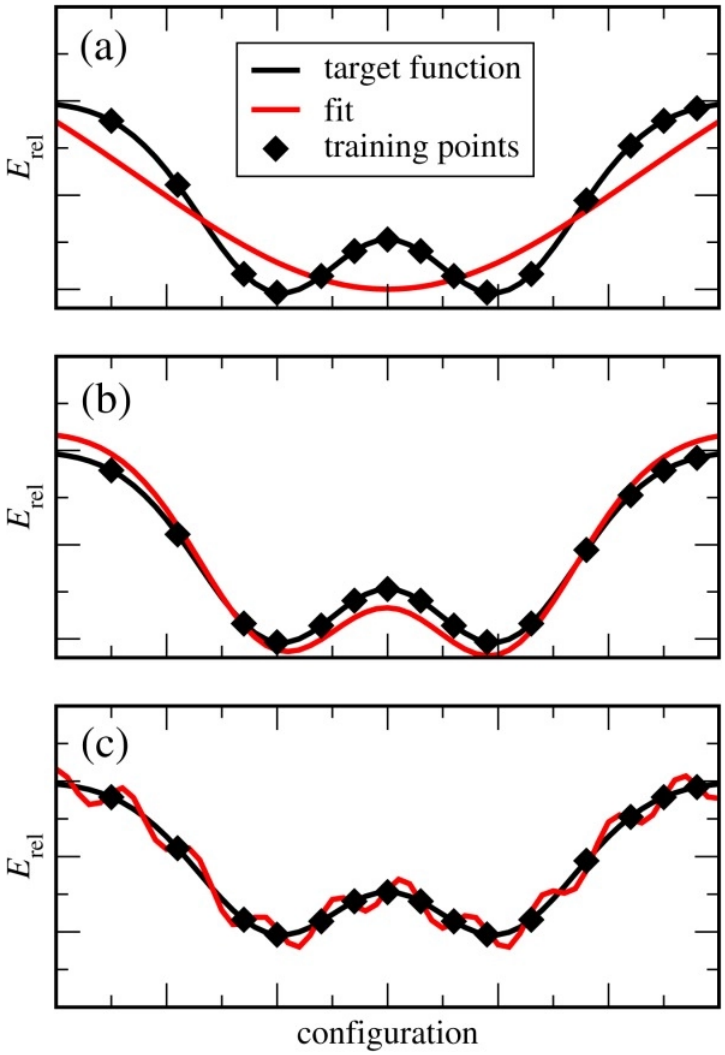

Fig. 2.6: (a) Underfitted neural network model (b) Well-fitted neural network model (c) Overfitted neural network model. (The figure comes from the reference [24].)

2.3 Classical nucleation theory

Classical nucleation theory (CNT) is employed to understand the nucleation process in a thermodynamical way. It can usually explain the condensation of a vapor or crystallization from a liquid. In homogeneous nucleation, it is assumed that a spherical nucleus is formed with a radius r. The change in the free energy of the system is given by

$$\Delta G(r) = -\Delta G_{\alpha\beta}\frac{4}{3}\pi r^3 + \sigma_{\alpha\beta}4\pi r^2 \tag{2.29}$$

where $\Delta G_{\alpha\beta}$ and $\sigma_{\alpha\beta}$ are the Gibbs free energy difference and the interfacial free energy between the phase α and β. In the Eq. (2.29), the first term represents the contribution by bulk free energy which is dominant with a large r. The second term is the penalty energy by the interface between the two different phases and dominant with small r. This behavior is sketched in Fig. 2.7. Since the probability of formation of the nucleus is dependent on ΔG, the nucleation hardly proceeds where $dG/dr = 0$. That is, the decaying and growing process of the nucleus is divided based on the critical radius (r^*) given by

$$r^* = \frac{2\sigma_{\alpha\beta}}{\Delta G_{\alpha\beta}}. \tag{2.30}$$

The nucleation barrier (ΔG^*) is calculated by inserting r^* into Eq. (2.29) and expressed by

$$\Delta G^* = \frac{16}{3}\frac{\sigma_{\alpha\beta}^3}{(\Delta G_{\alpha\beta})^2}. \tag{2.31}$$

When $r < r^*$, the small nuclei decay finally. When $r > r^*$, the nucleation process is favorable and the nuclei grow gradually. Then, the nucleation rate J can be expressed in the Arrhenius type. In addition, considering kinetic contribution together, the steady-state nucleation rate is followed by

$$J = A\exp\left(-\frac{\Delta G_D^*}{k_B T}\right)\exp\left(-\frac{\Delta G^*}{k_B T}\right) \tag{2.32}$$

where A is the prefactor and ΔG_D^* is the activation barrier for diffusion.

According to CNT, the change in the free energy ΔG is depending on the material-dependent physical quantities such as $\Delta G_{\alpha\beta}$ and $\sigma_{\alpha\beta}$. In a thermodynamical way, the change in the free energy between the liquid and crystalline phases ΔG_{lc} is given by

$$\begin{aligned} \Delta G_{lc} &= \Delta H_{lc} - T\Delta S_{lc} \\ \Delta H_{lc} &= \Delta H_f - \int_T^{T_m} \Delta C_p dT \\ \Delta S_{lc} &= \Delta S_f - \int_T^{T_m} \frac{\Delta C_p}{T} dT \end{aligned} \tag{2.33}$$

where T_m is the melting temperature, ΔH_f is a heat of fusion, ΔS_f is the entropy of fusion, and ΔC_p is the difference in specific heats of the two phases, which is defined as $(C_p^l - C_p^c)$. As experimental data for the heat capacity of the supercooled liquids is insufficient, ΔC_p can be approximated to a linear form by

$$\Delta C_p = AT + B \tag{2.34}$$

where A and B are constants. Then, ΔG_{lc} is rewritten by

$$\Delta G_{lc} = \frac{\Delta H_f \Delta T}{T_m} - \frac{1}{2} A(\Delta T)^2 + B\left(T \ln \frac{T_m}{T} - \Delta T\right) \tag{2.35}$$

where ΔT is the difference between the melting temperature T_m and the given temperature T. By employing a simple approximation that $\Delta C_p = 0$, we obtain

$$\Delta G_{lc} = \frac{\Delta H_f \Delta T}{T_m} \tag{2.36}$$

which is generally known as Turnbull approximation. [25] If the temperature dependence is negligible in ΔC_p, $A = 0$ and $B = \Delta C_p$, Eq. (2.35) is reduced to

$$\Delta G_{lc} = \frac{\Delta H_f \Delta T}{T_m} - \frac{\Delta C_p (\Delta T)^2}{T_m + T} \tag{2.37}$$

where $\ln(T_m/T) \approx 2\Delta T/(T_m + T)$. Here, Thompson and Spaepen suggested an approximation of heat capacity in terms of ΔH_f and T_m. [26]

$$\Delta C_p = \frac{\Delta H_f}{T_m} \tag{2.38}$$

This approximation is applied for Eq. (2.37), the change in free energy is simplified as

$$\Delta G_{lc} = \frac{\Delta H_m \Delta T}{T_m} \frac{2T}{T_m + T}. \tag{2.39}$$

For the interfacial energy σ_{lc}, a weak temperature-dependent behavior of the interfacial energy is usually approximated to a constant. Using the expression of Spaepen and Meyer [27]

$$\sigma_{lc} = \frac{\Delta H_m \alpha_m}{(N_A V^2)^{1/3}} \frac{T}{T_m} \tag{2.40}$$

where α_m is a constant which is geometrically computed to be 0.86. The value is based on the assumption that the interface is formed between a liquid and a cubic crystal. Here, it is reasonable to take T to be the glass transition temperature (T_g) for the phase change materials.

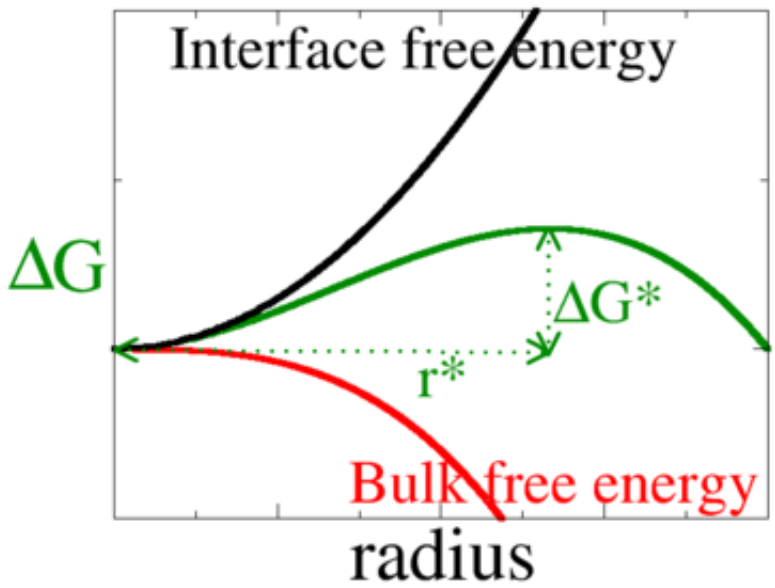

Fig. 2.7: A schematic free energy curves of homogeneous nucleation

Chapter 3

Crystallization of amorphous GeTe

3.1 Introduction

Understanding the crystallization behavior of the phase change materials is critical in PCM applications. Since the writing/erasing operations in PCM work by phase transition, the phase transition of the phase change materials is one of the interesting topics. In particular, the writing speed with recrystallization should be more improved in order that PCM will replace the conventional memories such as DRAM. In this regard, the crystallization kinetics of the phase change materials has been a subject of intensive studies in both experiment and theory.

In the case of the phase change materials with the switching speed of tens or hundreds nanoseconds, experimental research has some limitations to observe the crystallization moment. One is the difficulty in controlling temperatures. Crystallization occurs soon after the temperature goes above the glass transition temperature. Therefore, it is hard to study crystallization behavior in a wide range of the temperatures between the melting temperature and the glass transition temperature. In addition, we just know the power of the applied laser or electrical pulses. It is difficult to measure the temperature of the material exactly. The other issue is that observing crystallization process on the atomic scale is difficult due to scaling down of the device size. Experi-

ments have advantages of measuring physical properties like the melting temperature, the glass transition temperature, or growth velocity, but disadvantages of revealing the atomic scale behaviors of the materials.

On the theoretical side, a direct simulation for crystallization using AIMD is a powerful tool and have provided great insights for the crystallization behavior at the atomic scale. It is possible to track the changes in atomic structures with a time step of a few femtoseconds during AIMD. For example, one AIMD study showed that the medium-range order represented by fourfold rings plays a crucial role in fast crystallization of GST. [5] In addition, the effects of dopants in GST are explicitly investigated using AIMD simulations. It was demonstrated that Bi doping increases preference of the octahedral geometry which resembles to the building block of rocksalt GST, and makes the crystallization speed faster. [6] On the other hand, N doping increases the population of the tetrahedral geometry due to strong covalent bonding character, and hinders growth of crystal planes by distorting local lattice. [7] However, the simulation size is limited to a few hundreds of atoms due to the compuational cost and the disordered systems significantly suffer from finite-size effects. One recent study showed that even 460-atom of GST model is insufficient since the crystal growth velocity is overestimated about 2 times than that in 900-atom of GST model and the results from the 900-atom modeling are in a good agreement with experiment. [28] Still, nanosecond-scale simulations are unaffordable using AIMD.

Recently, machine learning techniques are employed to overcome the computational limitation of AIMD. [29] In this approach, general mathematical models such as neural network [30] and Gaussian process [31] are trained over *ab initio* energies, forces, or stresses and predict those quantities of untrained structures with computational speeds faster than *ab initio* calculations. The machine-learning approach to develop the classical interatomic potential is useful for systems with complicated bonding natures such as chemical reactions or phase transitions where the form of bonding natures is ill-defined. That is, the phase change materials are proper application. In

Refs. [32–38], the NNP was developed for a representative binary phase change material, GeTe and used in a variety of conditions to simulate the system size beyond the current capability of AIMD. In particular, the crystallization kinetics of *a*-GeTe models was investigated and the effects of temperature and interface were analyzed. [33, 34]

Among the results from the previous simulations of GeTe using the NNP [33], a critical point is noticed. In a wide range of temperatures between 500 and 650 K, the entire crystallization process (including nucleation and growth) is complete within 2 ns. This is not matched to the results of many AIMDs on GeTe and GST that show apparent incubation periods (the time span before appearance of supercritical nuclei [39]) of $0.1 \sim 2$ ns under high pressure conditions. [5–7, 39–44] The incubation-free crystallization is observed when a pre-existing crystalline seed is inserted in the amorphous models. [45] That is, it seems that the nucleation barrier in the NNP may be underestimated. In addition to AIMD simulations, the fastest crystallization time is reported to about 30 ns for melt-quenched amorphous GeTe samples in laser-pulse experiments. [46, 47] The electrical-pulse experiment on GST also showed that the phase transition takes at least 10 ns. [48–50] Since the maximum growth velocity in Ref. [33] is just about two times higher than the measured value [51], it is considered that the nucleation rate might be exaggerated in the previous simulations. Although it is reported that crystallization in the PCM with the thin GeTe layer is complete within only 1 ns [52], this is because the amorphous GeTe is surrounded with the crystalline rim, which leads to a growth-dominated crystallization.

In this chapter, the structural features of the amorphous GeTe are analyzed to address and resolve the above issue in the NNP. It is found that the planarity of fourfold rings, which represents the medium-range order, is overestimated by the NNP, resulting in a low nucleation barrier. We find significant improvements in the medium-range order by adding ring relaxation trajectories by DFT into the training set of the NNP. Using the improved NNP, the crystallization simulations are successfully performed

under the condition close to realistic systems. In the following section, we discuss details on training NNP and simulation setup suggest an approach to improve NNP. The structural property and crystallization behavior by the improved NNP are also analyzed and discussed.

3.2 Computational details

3.2.1 Training set

We train NNP over reference structures composed of various liquid, amorphous, and crystalline structures. The detailed information of the training set is summarized in Table 3.1. Here, a few meV/atom (or tens of meV/Å) of variations in root-mean-square errors (RMSE) are observed but negligible. The size of errors can result from a random initialization of weights in the neural network model and a stochastic character of training the neural network model.

Except for ring relaxation data, all the structures are sampled from trajectories of AIMD which is performed with Vienna *Ab initio* Simulation Package (VASP). [53, 54] The Perdew-Burke-Ernzerhof functional is chosen to describe exchange-correlation functional [18] and the cutoff energy of the plane-wave basis set is chosen to 200 eV for cost-effective AIMD. The total energies and atomic forces for the reference structures are calculated again to improve accuracy by setting the cutoff energy of 400 eV and the spacing of **k**-point grid mesh smaller than 0.1 π/Å. This calculation setup ensures the convergence of the total energy and the atomic forces to below 1 meV/atom and 0.05 eV/Å, respectively.

In Table 3.1, in addition to the usual structures with stoichiometric GeTe, some structure types in the training set are involved to improve the accuracy and reliability of NNP. First, the melting process of crystal GeTe is expected to provide information for the energy barrier between liquid and crystal phases. Without the melting data, partially crystallized structures are often observed during quenching. In addition, the crystallization of amorphous GeTe can be learnable as shown in Fig. 3.1. [55] For short validation of the NNP, 96-atom amorphous structures are generated by the melt-quench method and crystallization simulations are performed at 600 K for 2 ns with the simulation cell fixed to the crystalline density. Figure 3.1 (a) compares the potential energy surface of DFT and NNP along the crystallization trajectory, and (b) and (c)

Table 3.1: Summary of reference structures and root-mean-square errors (RMSEs) for the validation set.

Structure type	Number of structure	Number of training points	RMSE_{energy} (meV/atom)		RMSE_{force} (eV/Å)	
			c-NNP	m-NNP	c-NNP	m-NNP
Crystal	504	28,471	3.14	2.48	0.16	0.17
Liquid	500	48,000	4.41	4.05	0.26	0.28
Amorphous	251	24,096	7.24	6.20	0.26	0.28
Quenching ($1000 \rightarrow 300$ K)	518	49,728	5.81	3.67	0.25	0.27
Melting (FCC $\rightarrow$ liquid)	352	33,792	5.11	3.47	0.23	0.26
Mixding liquid (Ge + Te)	301	57,920	3.75	3.07	0.26	0.30
Liquid (Ge or Te)	375	37,500	3.92	3.48	0.26	0.27
Ring relaxation	774	74,304	-	3.54	-	0.16
Total	3,575	347,711	4.99	3.65	0.24	0.25

show the force errors of the NNP. Though a constant energy shift of 25 meV/atom is observed, the shifted potential energy surface is matched to DFT. RMSE for forces is computed to 0.27 eV/Å, which is within a reasonable range. Therefore, it seems that the melt-quench and crystallization simulations by the NNP is reliable.

Secondly, it is found that during liquid simulations at 1000 K, phase separation into unary Ge and Te often occurs when the training set consists of only 1:1 composition. It is attributed to ad hoc energy mapping in the GeTe system [55], which can induce the instability of NNP. To reduce the ad hoc energy mapping, the connectivity between data points should be maintained. Since the mixing data is prepared by sampling MD trajectories of diffusional mixing from unary Ge and Te liquids shown in Fig. 3.2 (a), the data points are close enough to one another. Principal component analysis (PCA) is applied to show the distribution of the data points in reduced dimensions. Figure 3.2 (b) explicitly shows a distribution of the data points on the first (PC1) and second principal components (PC2) with distinct color for each subset. PC1 and PC2 mean the axes where the data points are projected to have the first and second-largest variance. The connectivity of the unary (purple) and binary (green) liquid data is maintained through the mixing data (red). This precludes the unphysical phase separation and increases the stability of NNP.

Finally, the ring relaxation data in Table 3.1 is prepared to refine the medium-range order structures in amorphous GeTe described by the NNP. Unlike other data set, the initial structures are obtained by NNP and relaxed within the DFT framework. The detailed effects of the ring relaxation data will be discussed later.

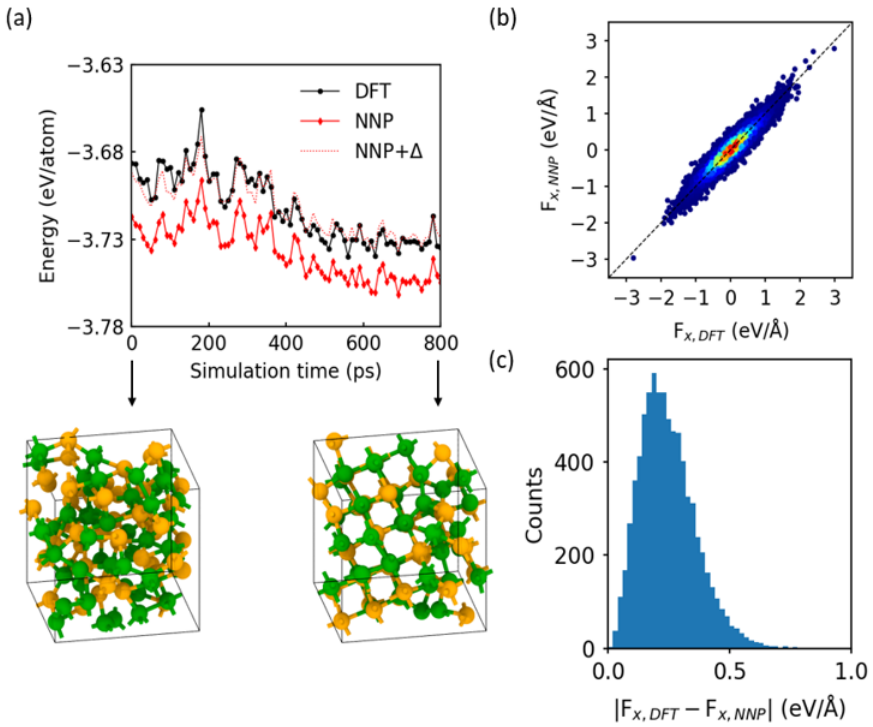

Fig. 3.1: (a) Comparison of PES of crystallization trajectory generated by NNP with DFT. The constant energy shift Δ of $\sim$ 25 meV/atom is observed, but the relative potential energy surfaces are close to each other. (b) The correlation of the atomic forces for each component (x,y, and z). The dense region is colored in red while the color of the sparse region is close to blue. (c) Histogram of the errors in the atomic forces.

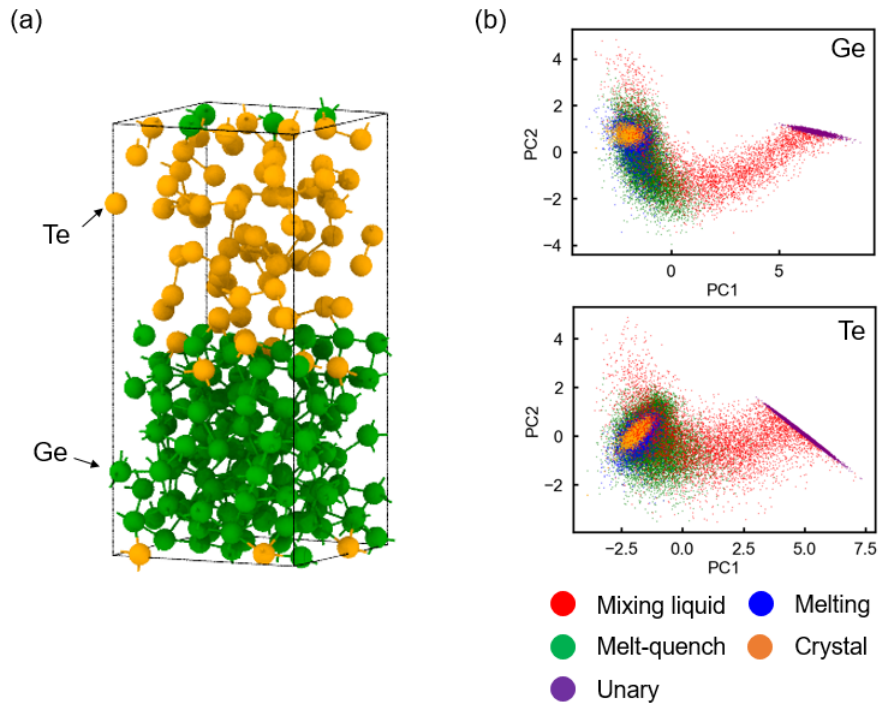

Fig. 3.2: (a) The initial slab model for the mixing data. (b) Distribution of the training points of each structure type in PCA space. PC1 and PC2 means that the first and second largest variance along the axis.

3.2.2 Training method

The NNP is trained using SIMPLE-NN (SNU Interatomic Machine-learning PotentiaL packagE-version Neural Network). [56] The architecture of the neural network model is 70-30-30-1 and atom-centered symmetry functions are used as input features describing the local environment around an atom. [57] The symmetry functions consist of 16 radial and 54 angular symmetry functions with a cutoff radius of 7 Å. The parameters for each symmetry function are taken from Ref. [58]. Since the atom-centered symmetry functions are highly correlated with one other, the decorrelating process is performed by PCA without any reduction of dimensions. After applying PCA, all the components are further normalized by dividing its variance, which is called whitening. It accelerates the accuracy and convergence of training. The loss function for training is defined as the sum of the square of RMSEs for energy and force. Additionally, L2 regularization term with a coefficient of 10^{-8} is appended to prevent undertraining of the ring relaxation data and unexpected overfitting. The coefficient is determined via parameter tests as shown in Fig. 3.3. One-fifth of the entire training data is randomly chosen and constructs a validation set. Others constitute a training set. The learning curves for NNP are shown in Fig. 3.4.

In this chapter, two types of NNP are developed. The one, named as c-NNP, is constructed by using the reference structures in Table 3.1 except for the ring relaxation data. It is validated if the c-NNP reproduces the incubation-free crystallization observed in the previous literature. To improve this, the ring relaxation data is added to the training set. This modified NNP is called as m-NNP. The RMSEs for energy and force in the validation test are tabulated in Table 3.1 and are under 5.0 meV/atom and 0.3 eV/Å, respectively.

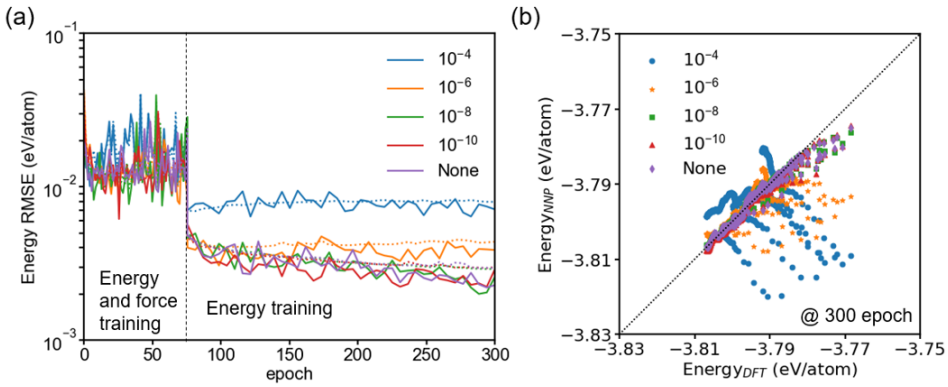

Fig. 3.3: (a) Learning curves of NNP and (b) Energy correlation plots of the ring relaxation data with L2 regularization coefficients.

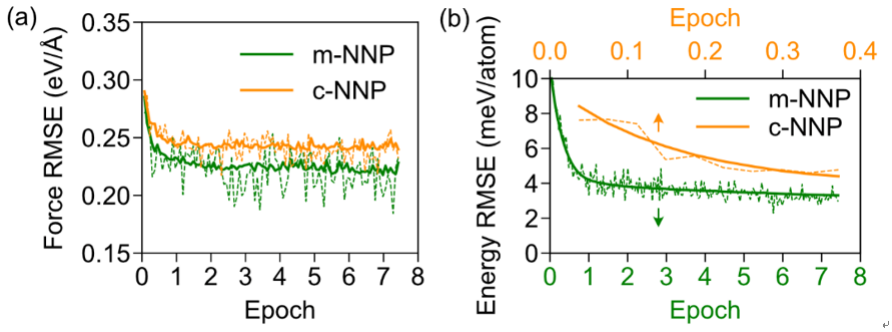

Fig. 3.4: Learning curves of NNP for (a) force and (b) energy. The solid lines and dashed lines indicate the RMSEs of the validation and training data, respectively.

3.3 Validation

3.3.1 Bulk properties of crystalline phases

Birch–Murnaghan equation of state in Eq. (3.1) is a simple equation to simulataneously show important bulk properties such as equilibrium volume (V_0), minimum energy (E_0), and bulk modulus (B).

$$E(V) = E_0 + \frac{9V_0B_0}{16}\left\{\left[\left(\frac{V_0}{V}\right)^{\frac{2}{3}} - 1\right]^3 B_0' + \left[\left(\frac{V_0}{V}\right)^{\frac{2}{3}} - 1\right]\left[6 - 4\left(\frac{V_0}{V}\right)^{\frac{2}{3}}\right]\right\} \tag{3.1}$$

The two types of NNPs are validated by comparing the bulk properties of crystalline GeTe calculated by DFT. The equilibrium volumes for hexagonal and fcc GeTe are 28.03 and 27.29 Å^3/atom in DFT, respectively. Those in c-NNP (m-NNP) are 27.82 (28.10) and 27.10 (27.4) Å^3/atom. The energy differences between the phases are 0.14 eV/atom in DFT, 0.12 eV/atom in c-NNP, and 0.18 eV/atom in m-NNP. The minimum energy and the energy difference between the two phases are important quantities, especially for crystallization. As shown in Fig. 3.1, the equilibrium volumes and minimum energies for each phase are well reproduced by NNPs. Bulk modulus is calculated by fitting the energy-volume data to Eq. (3.1). The bulk moduli calculated using DFT are 46.2 GPa for hexagonal GeTe and 48.8 GPa for fcc GeTe. The bulk modulus of hexagonal GeTe are 58.0 and 52.5 GPa and those of fcc GeTe are 55.9 and 43.3 GPa in c-NNP and m-NNP, respectively. Since local environments in the crystalline state are simple and little changed, it is seen that the training data is well prepared to reproduce the bulk properties of the crystalline GeTe.

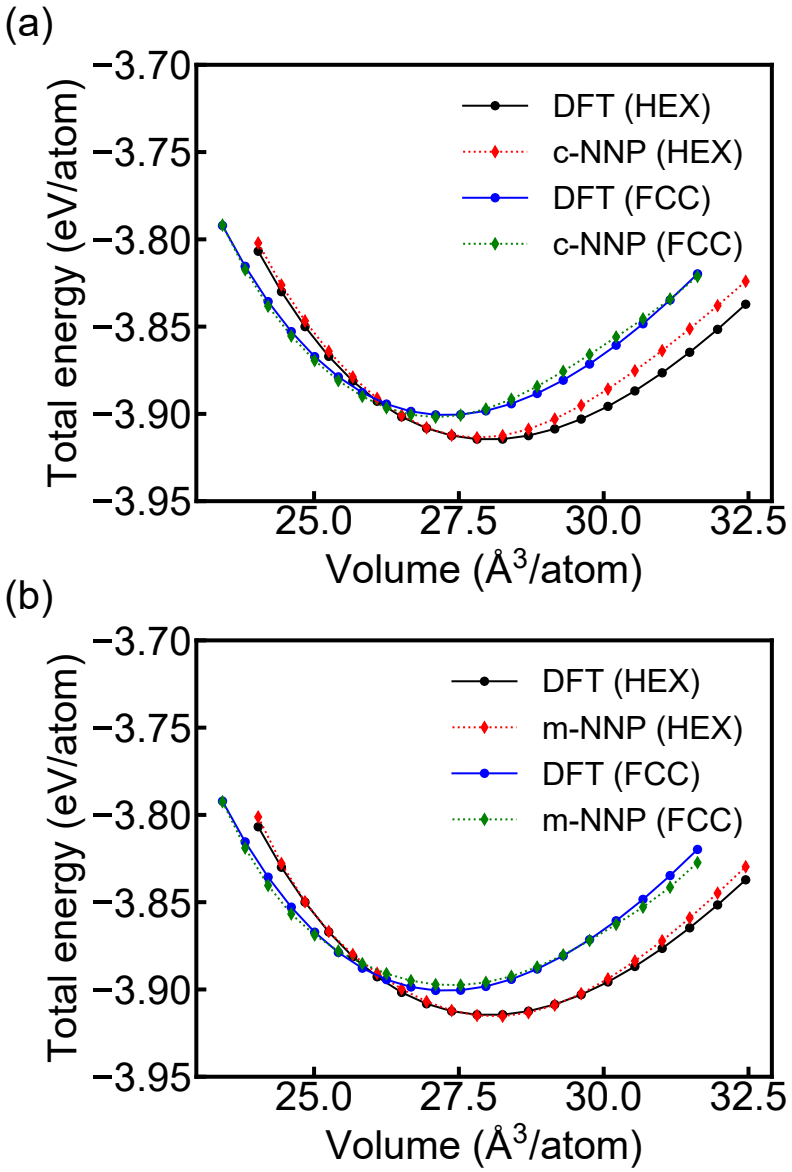

Fig. 3.5: Birch-Murnaghan equation of state for hexagonal (HEX) and fcc (FCC) GeTe. Solid lines represent DFT data and dashed lines (a) c-NNP data and (b) m-NNP data, respectively

3.3.2 Bulk properties of liquid phase

In the melt-quench method, amorphous structures are obtained by quenching of liquid structures at high temperatures (higher than melting temperature). In general, the amorphous structures are considered as a supercooled liquid state due to rapid quenching speed in simulations with respect to experiments. Therefore, the reliability of the amorphous structure is highly dependent on that of the liquid structure.

Liquid GeTe is generated by AIMD simulation. Initial atoms are randomly sprayed in the cubic box whose density is set to 34.5 atoms/nm^3 which is a measured density of amorphous. [59] The generated structure is equilibrated at 1500 K for 5 ps and 1000 K for 30 ps. Since the melting temperature of GeTe is 998 K, [60] GeTe at 1000 K should be liquid. The structures equilibrated in DFT are used for the starting structures of melt-quench simulations in NNP. After equilibration at 1000 K, structural properties of liquid GeTe are evaluated using RDF and ADF representing average local environments. In Fig. 3.6, total RDF and ADF of both NNPs are in good agreement with those of DFT. The first peak positions, heights, and widths of partial RDFs of Ge-Ge, Ge-Te, and Te-Te are closely reproduced by the NNPs. The first peaks of Ge-Ge are located at 2.73, 2.73, and 2.73 Å and those of Ge-Te are positioned at 2.84, 2.84, and 2.82 Å in DFT, c-NNP, and m-NNP, respectively. In particular, DFT, c-NNP, and m-NNP produce the main peak around 90° and a shoulder peak around 60°.

Diffusion coefficients (D) are computed from the slope of the mean square displacement (MSD, $\left\langle \Delta \mathbf{r}^2 \right\rangle$), which is related to the kinetics of crystal growth.

$$D = \frac{\left\langle \Delta \mathbf{r}^2 \right\rangle}{6t} \tag{3.2}$$

In DFT, diffusion coefficients of Ge and Te are estimated to 5.12×10^{-5} and 3.47×10^{-5} cm^2/s, respectively. Other DFT study reported that the values are 4.65×10^{-5} for Ge and 3.93×10^{-5} cm^2/s for Te. [40] For c-NNP (m-NNP), the diffusion coefficients are estimated to 5.40×10^{-5} (5.46×10^{-5}) for Ge and 3.58×10^{-5} (3.84×10^{-5}) cm^2/s for Te, which is very close to the values in DFT.

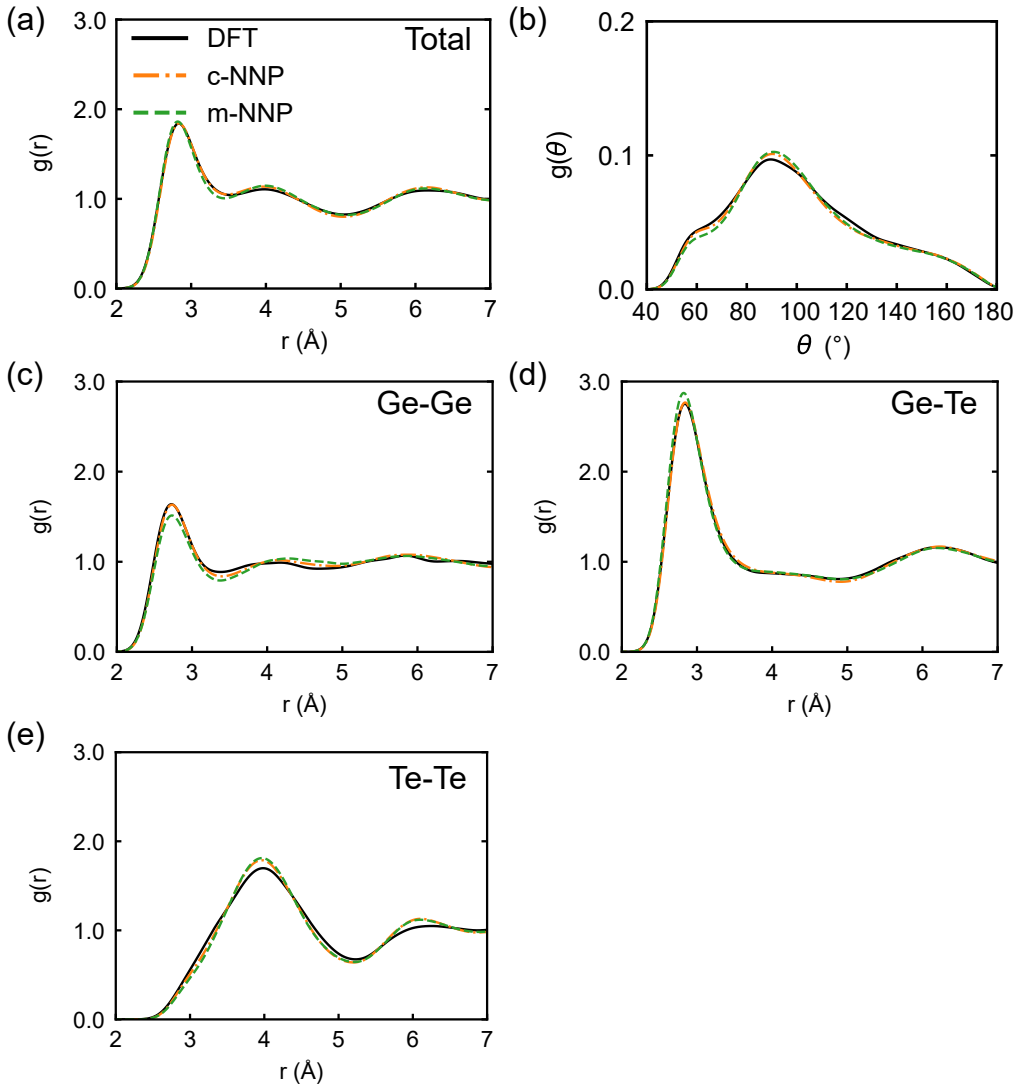

Fig. 3.6: (a) Total RDF, (b) total ADF, and (c) partial RDFs of Ge-Ge, Ge-Te, and Te-Te of DFT, c-NNP, and m-NNP. ADF is compurted with bond length of 3.2 Å.

3.3.3 Bulk properties of amorphous phase

Amorphous GeTe is obtained by quenching the liquid structures from 1000 K to 300 K with the rate of -15 K/ps. For a fair comparison, five 96-atom models are generated independently using DFT, c-NNP, and m-NNP. The structural properties are analyzed after geometry optimization with the volume and shape of the cells and atomic coordinates. The average density of relaxed structures using c-NNP (m-NNP) is 31.2 (31.9) atoms/nm^3, matching to that of DFT (31.9 atoms/nm^3). The energy difference between an amorphous structure and fcc crystal is 99 and 90 meV/atom in DFT and m-NNP, respectively.

RDFs and ADF of amorphous GeTe are presented in Fig. 3.7 and compared among DFT,c-NNP, and m-NNP. Figure 3.7 (a) and (b) show total RDF and ADF of the a-GeTe at 300 K and Fig. 3.7 (c) shows partial RDFs of amorphous GeTe at 300 K. The coordination numbers, computed by integrating RDF within 3.2 Å, are 3.94, 3.94, and 3.97 for Ge and 3.09, 3.02, and 3.10 for Te in DFT, m-NNP, and c-NNP, respectively. Compared to c-NNP, the first peak of Ge-Ge and the second peak of Te-Te bond are improved by m-NNP; the first peak position of Ge-Ge is 2.67 Å (2.72 Å in c-NNP), which is close to 2.65 Å in DFT. While the position of the second peak of Te-Te is similar between DFT (4.15 Å), m-NNP (4.09 Å), and c-NNP (4.13 Å), the height of the second peak (2.60 in DFT) is improved in m-NNP (2.72), compared to c-NNP (3.08). However, it is found that the sharpened second peak in RDF and the overestimated peak around 90° in ADF remain.

The fine details of the medium-range order are analyzed using ring statistics and geometry. The number of primitive rings is computed by R.I.N.G.S. code [61] and ring distributions are shown in Fig. 3.8. The overall ring distribution of m-NNP is close to that of DFT. In particular, the fraction of ABAB-type (A=Ge and B=Te) within fourfold rings is about 80% for m-NNP and DFT (see hatched regions). In c-NNP, this fraction is 86%, slightly overestimated. Fig. 3.9 (a) shows distributions of the inter-diagonal distance in fourfold rings. The average value of d is 0.43 Å for m-NNP,

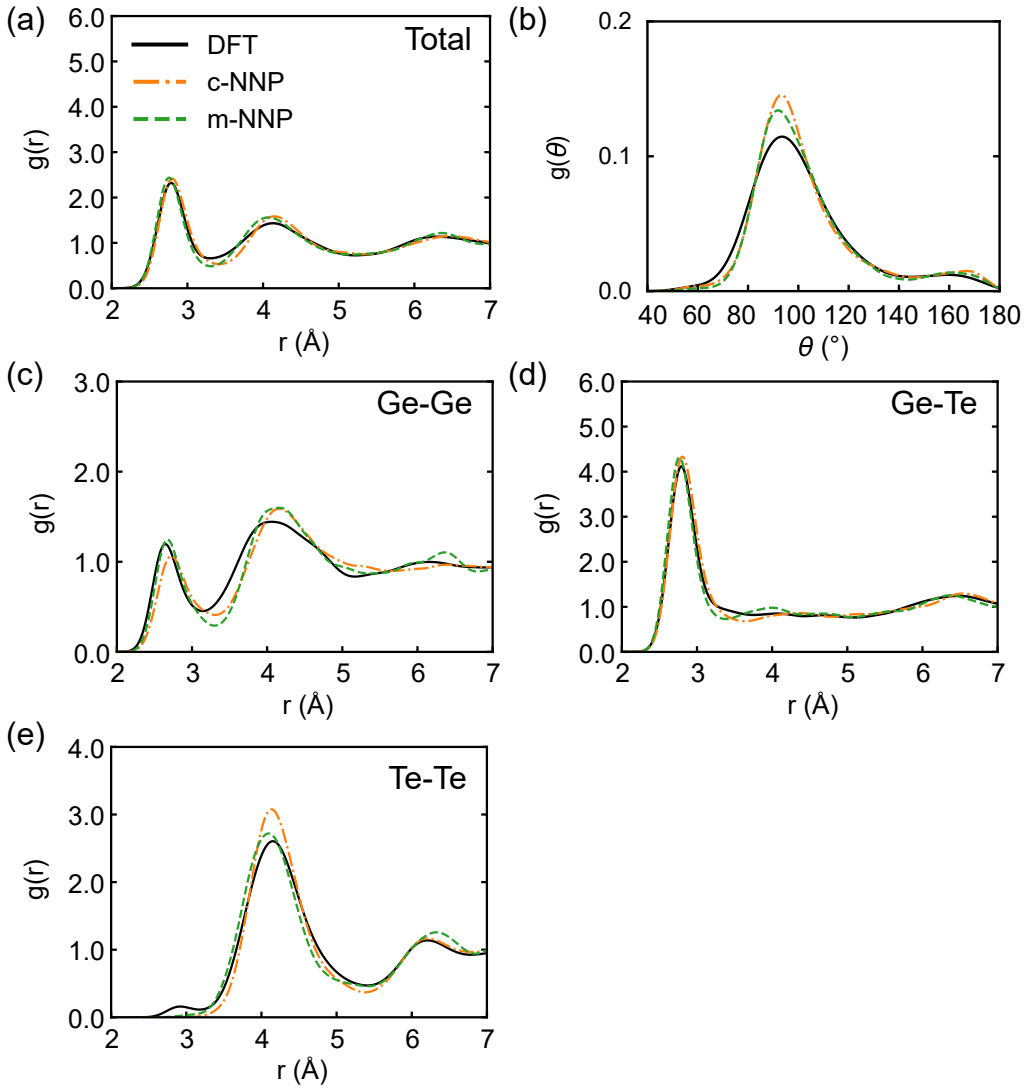

Fig. 3.7: (a) Total RDF, (b) total ADF, and partial RDFs of (c) Ge-Ge, (d) Ge-Te, and (e) Te-Te of DFT, c-NNP, and m-NNP. ADF is computed with bond length of 3.2 Å.

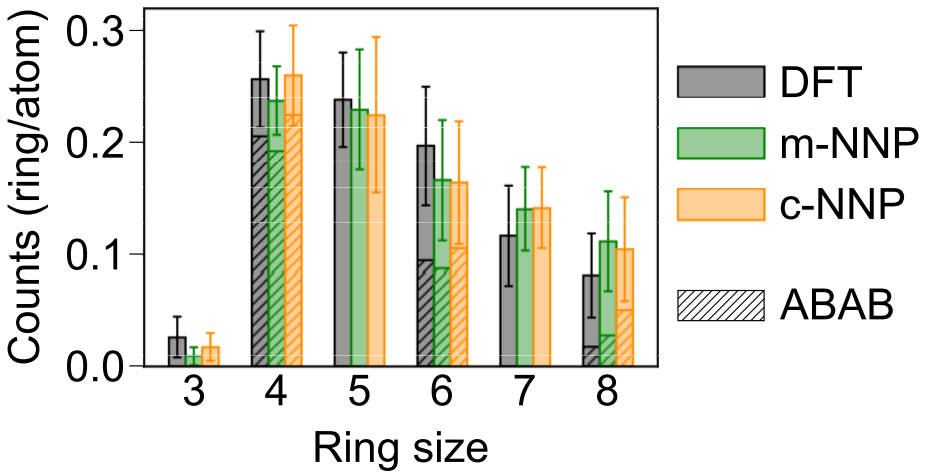

Fig. 3.8: Ring statistics of amorphous GeTe at 300 K. Bonds within 3.2 Å are considered.

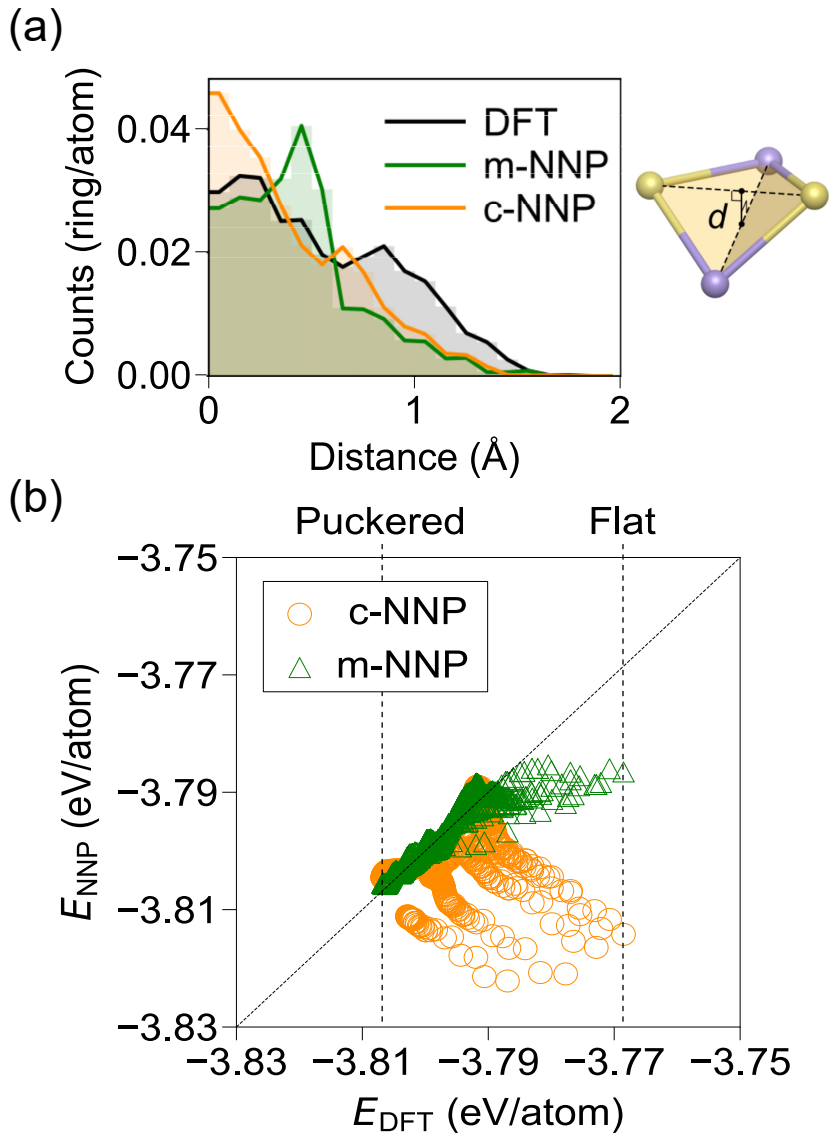

Fig. 3.9: (a) Planarity of the fourfold rings in amorphous GeTe at 300 K. Bonds within 3.2 Å are considered. (b) The energy correlation between DFT and NNP for five DFT-relaxed trajectories of amorphous GeTe generated by c-NNP. High-energy structures (marked as 'Flat') in DFT contain fourfold rings with small d values that increase as the structure relaxes to low-energy one (marked as 'Puckered').

showing that the distribution shifts away from zero compared to c-NNP. Although highly distorted fourfold rings ($d < 0.50$ Å) are still suppressed than in DFT, the number of the planar fourfold rings ($d < 0.25$ Å) is almost the same as that of DFT. The corresponding distributions at 500 K and various density conditions are presented in Fig. 3.9 and they are consistent with Fig. 3.9.)

Additionally, we calculate interfacial energies between crystal and amorphous phases (σ_{ac} in Eq. (2.29)) by following the method in Ref. [62]. A pre-ordered crystalline seed with a certain radius is inserted in amorphous GeTe and the overlapping or too close atoms are removed at the same time. At a given temperature, it is checked if the seed grows or decays during NVT simulations. Then, we can estimate the critical size of the spherical nucleus at the given temperature and critical temperature for a specific size of the nucleus. One snapshot of the model and the estimated critical temperatures with the nucleus size is shown in Fig 3.10. A relation between ΔT and r^* can be obtained by inserting Thompson-Spaepen expression (Eq. (2.39)) into Eq. (2.30).

$$\Delta T = \frac{\sigma T_m}{\Delta H} \left(\frac{T_m + T}{T} \right) \frac{1}{r^*}. \tag{3.3}$$

The interfacial energy (σ) can be estimated by fitting the data to Eq. (3.3) and the values are 0.062 and 0.075 J/m^2 in c-NNP and m-NNP, respectively. (For comparison, σ of GST was experimentally estimated to be 0.075 J/m^2 by applying Eq. (2.40). [27, 63]) Combined with Eq. (2.31), this indicates that m-NNP may have larger nucleation barriers than c-NNP. Therefore, it is expected that the issue of fast crystallization would be resolved by m-NNP as medium-range as well as short-range orders are captured properly. The results for crystallization simulations using m-NNP will be presented in the next section.

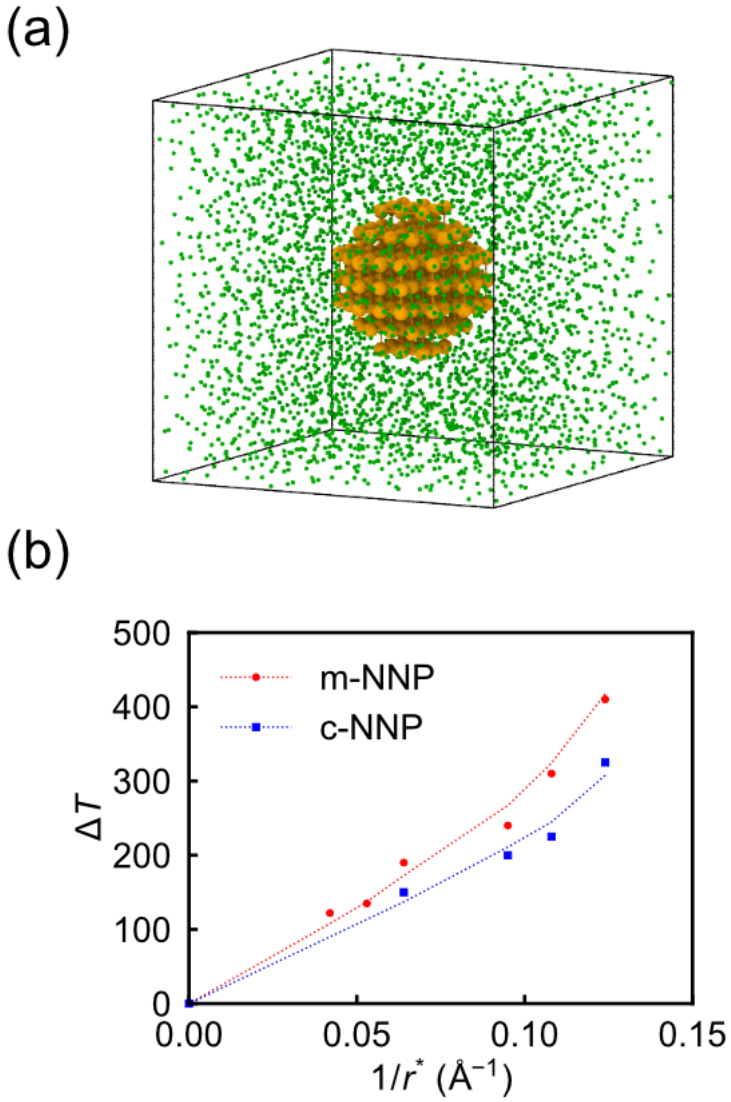

Fig. 3.10: (a) A snapshot of the model with radius of the crystalline seed 10 Å. The green atoms are amorphous GeTe and the orange atoms are the inserted crystalline atoms. (b) Difference between the critical temperature and the melting temperature as a function of the inverse size of the crystalline seed.

3.4 Crystallization simulation

In the PCM device, only some of the phase-change region is actively changed. HRTEM images clearly show the dome-like switching region on the bottom gate. [64] This device condition is usually observed in continuum modeling, not atomic-scale modeling. [65] However, the simulations using AIMD have been carried out under the limit condition because demanding computational costs are required to handle a few hundreds of atoms for nanoseconds. To accelerate crystallization, the density of the simulation cell is usually fixed to the crystalline density. It is found that the equilibrium volume of the amorphous state V_a is expressed in terms of bulk modulus of crystal and amorphous (B_c and B_a), the bulk atomic volume of amorphous (V_c and V_a^0), and the total and switching volume of the phase-change region (V_T and V_c) assuming the hydrostatic pressure followed by

$$\frac{V_a}{V_a^0} = \frac{B_a(V_T - V_c) + B_c V_c}{B_c V_a^0 + B_a(V_T - V_c)}. \tag{3.4}$$

This relation indicates that when V_c is equal to V_T, the equilibrium volume of amorphous V_a is equal to the total phase-change volume, which is a fully amorphized state. Furthermore, since the phase-change region is crystallized in the fabrication process, the total volume of the phase-change region has the crystalline density. Therefore, it is considered that the limit condition of crystallization simulation in AIMD is considered as a fully amorphized condition. In practice, less than 10% of the whole region is actively switched. [64, 65] Herein, the partially amorphized condition close to device condition is set assuming 10% of the whole phase-change region is actively changed. The physical quantities required for Eq. (3.4) and calculated equilibrium volumes of the amorphous region under two conditions are summarized in Table 3.2.

Table 3.2: The calculated equilibrium volumes of the switching amorphous region with volume and bulk modulus of crystalline and amorphous GeTe.

	V_a^0 (Å^3/atom)	B_a (GPa)	B_c (GPa)	V_a (Å^3/atom) $[V_c/V_T = 1.0]$	V_a (Å^3/atom) $[V_c/V_T = 0.1]$
DFT	31.33	13.3	48.8	27.3	30.06
c-NNP	32.08	11.8	55.9	27.1	29.65
m-NNP	31.35	7.2	43.3	27.4	29.62

3.4.1 Equilibrium volume condition

When it is assumed that about 10% of the cell volume transformed into amorphous GeTe, the density of the amorphized region is set to the value in Table 3.2. Under the partially amorphized condition, crystallization simulations using m-NNP are carried out. (There are two runs at 500 K.) Within 20 ns, the crystallization is completed only at 500 K. The incubation period, in this case, is as long as 7 or 17 ns, a time scale comparable to the experiments. [46, 47] The large difference between two runs reflects the stochastic nature of nucleation and finite-size effects of the present simulation cell. This indicates that the crystallization of amorphous GeTe at this condition is nucleation-limited, rather than growth-limited. At higher temperatures, the nucleation is retarded because ΔG_{ac} is reduced and therefore, the nucleation barrier increases following Eq. (2.31).

It is seen that a single crystalline grain grows almost isotropically. The growth speeds are 1.31 and 3.82 m/s for the two runs, respectively, which are similar to 1.89 m/s for c-NNP. We also estimate growth speeds at 550–650 K by taking snapshots from 500 K simulation including a supercritical nucleus and annealing them at the elevated temperatures, since supercritical nucleus is not observed at these temperatures during the present simulation time. The calculated growth speeds are 2.58, 3.77, and 3.86 m/s at 550, 600, and 650 K respectively, which agrees reasonably with Ref. [33] (1.88, 3.60, and 5.12 m/s, respectively) as well as results by c-NNP.

After the crystallization completes, we analyze the defects within the crystalline grain and find that the defect density is 5% and antisite defects GeTe, and consequently Ge-Ge homopolar bonds, are the most frequent. As a result, the composition of the crystalline region becomes $Ge_{51}Te_{49}$ which is slightly Ge-rich. This is in a good agreement with the spectroscopic measurement that estimates 10% of Ge-Ge bonds and Ge vacancies in crystallized GeTe films. [66]

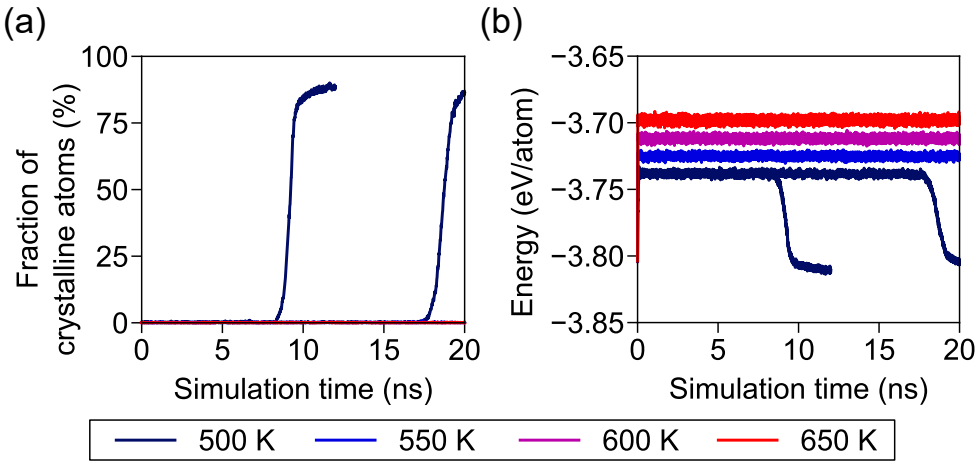

Fig. 3.11: (a) Time evolution of the percentage of crystalline atoms in 4096-atom cells and (b) the potential energy during the crystallization at 500, 550, 600, and 650 K with the density corresponding to the device condition (33.7 atoms/nm^3).

3.4.2 Crystalline volume condition

As the limit condition for crystallization, the density of the simulation box is set to the crystalline density. The starting amorphous structure consisting of 4096 atoms is obtained by the melt-quench process where the density is fixed. After quenched to 300 K, internal coordinates of atoms in the amorphous structure are optimized. The initial amorphous structure is independently heated to 500, 550, 600, and 650 K. Figure 3.12 shows that the crystallization is completed within 4 ns at all the temperatures. This is mainly because the incubation time is decreased substantially, but still the incubation time of $\sim$ 500 ps at all temperatures. As the pressure is increased, we find that the population of planar fourfold rings increases, which may lower the nucleation barrier. At 500 K, we observe four nuclei, implying that the nucleation is facile.

Since the crystallization proceeds at all temperatures, growth velocities are measured and shown in Fig. 3.13. For comparison, the crystalline growth speed at this temperature is 0.5 m/s, much smaller than at the device condition. This is because atomic migration is suppressed at higher densities.

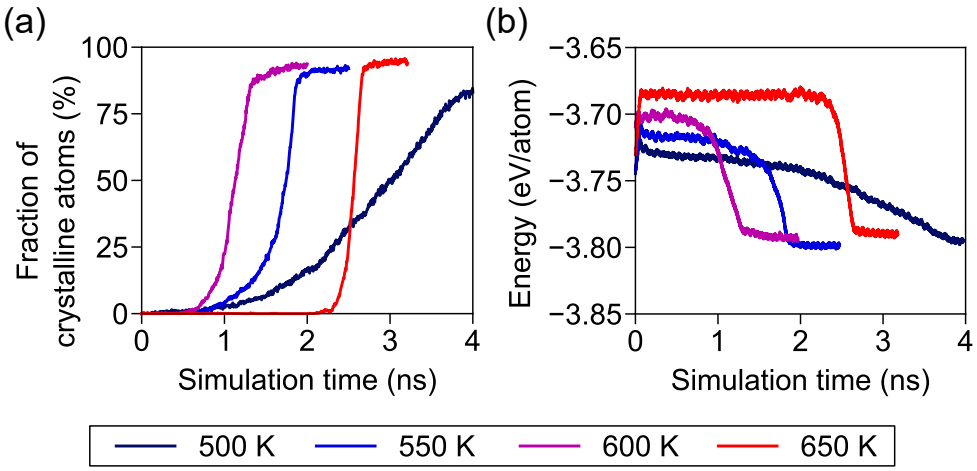

Fig. 3.12: (a) Time evolution of the percentage of crystalline atoms in 4096-atom cells and (b) the potential energy during the crystallization at 500, 550, 600, and 650 K with the density corresponding to the crystalline density (36.6 atoms/nm^3).

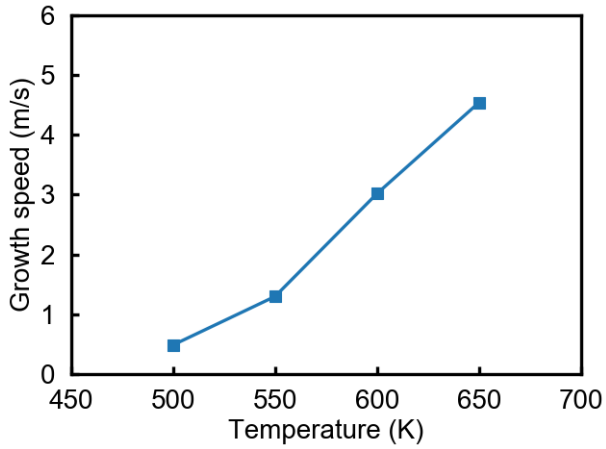

Fig. 3.13: Temperature-dependent growth velocity under fully amorphized condition.

3.5 Summary

Two types of NNPs are developed to investigate the atomic-scale crystallization behavior of GeTe. It was found that NNP trained with the usual training set reproduced satisfactorily the overall structural properties of liquid and amorphous GeTe at the DFT level. However, overly flat fourfold rings significantly shortened the incubation time, which is not compatible with experiments and *ab initio* simulations. By including the relaxation path from flat to puckered fourfold rings explicitly, we were able to generate an improved NNP that produces medium-range orders that are more consistent with DFT. Using the modified NNP, crystallization simulations were performed at two densities representing partially and fully amorphized devices, and temperatures ranging from 500 to 650 K. At both densities, the finite incubation time was observed. In particular, the incubation time under the partially amorphized condition was 7 or 17 ns, in reasonable agreements with experiments. However, the significant fluctuation in the incubation time implies that the present simulation is still limited by the finite size and a much larger simulation cell is needed for a systematic analysis on the temperature-dependent incubation time. In conclusion, by suggesting an efficient method to develop NNPs addressing the medium-range order, this work will contribute to simulating phase change materials more accurately and realistically.

Chapter 4

Al- and Ga-doped $Ge_2Sb_2Te_5$ (GST)

4.1 Introduction

Despite the excellent performance of GST in the PCM, further improvements are required in data retention, power consumption, and switching speed to compete with the conventional memory. One general and effective approach to modifying the relevant properties is doping. Up to this time, various kinds of dopants such as C, [67–73] N, [7, 74–80] O, [76, 77, 80, 81] Al, [82–84] Si, [80, 85–87] Sc, [88] Ti, [88] V, [88, 89] Cr, [88–92] Mn, [88, 89, 92–95] Fe, [88, 89, 96, 97] Co, [88, 92] Ni, [49, 88, 89, 92] Cu, [88, 89] Zn, [88, 89, 95, 98, 99], Ga, [100] Ag, [101–104] In, [105, 106] Sn, [106–108] and Bi, [6, 106, 108, 109] have been investigated. These dopants can be categorized based on their chemical features. One is p-block class (C, N, O, and Si), another is transition metal class (Sc, Ti, V, Cr, Mn, Fe, Co, Ni, and Cu), and the other is post-transition metal class (Al, Zn, Ga, Ag, In, Sn, and Bi).

A lot of experiments reported that p-block elements like C, N, O, and Si enhance the stability of amorphous GST (a-GST). They increase the crystallization temperature and activation barrier for crystallization. [67–70, 74–77, 85–87] They also hinder the grain growth and reduce the grain size, which leads to the reduction of the reset current and power. [67, 69, 74–76, 85, 86] The electrical resistance in the crystalline state is

increased since the p-block dopants increase in the structural disorder and band gap. However, it was reported that N, O, and Si dopants in GST induce the phase separation degrading the cyclability.[76–79] According to DFT calculations, the p-block dopants mainly enhance the covalency of Ge atoms and distort cubic or planar structures in the amorphous state, which makes the crystallization process slow. [7, 71–73, 80]

Transition metal dopants in the first row ($3d$) have been investigated for spintronics applications. The Fe-doped Ge-Sb-Te alloy showed a contrast magnetic property as well as electrical and optical properties between crystalline and amorphous states. [96] The Cr- and Mn-doped GST also showed different magnetic hysteresis loops. [90, 91, 93, 94] In addition to the magnetic property, the transition metal dopants make the temperatures for 10-year-data retention higher. In DFT studies, V, Cr, Mn, and Fe dopants can generate stable magnetic states. [88, 89, 92, 95, 97]

Finally, the post-transition metal dopants exhibit various effects on GST. For Al, Zn, and Ga, it was reported that the dopants enhance the thermal stability of the a-GST and increase the band gap, whose effects are similar with p-block elements. [82, 83, 98–100] On the other hand, In, Sn, Ag, and Bi reduce the crystallization temperature and time. [101, 105, 107, 109] In the case of Zn, Ag, and Bi, DFT calculations were performed and it is found that the local configuration of Zn is largely shifted from tetrahedral to octahedral coordination during the crystallization [95] while Ag doping reduces the phase transition time and the optical gap, consistent with the experiment. [104] Bi doping enhances the crystallization speed by stabilizing planar structures around Bi. [6]

Among the previous studiess, the effects of the small-size post-transition metal dopants such as Al and Ga were still vague, even though they have a large potential to tune the properties of GST. [82–84, 100] In this regard, we investigate the effects of Al and Ga dopants theoretically. We investigate the structural changes in a-GST by doping and try to establish a relation between them and crystallization behaviors. Doped amorphous GST structures are obtained via melt-quench simulations. We find

that Al and Ga dopants in a-GST behave similarly as they are coordinated with four Te atoms in a tetrahedral geometry. Since dopants form bonds with a large numbers of Te atoms, the number of homopolar bonds of Ge-Ge, Ge-Sb, and Sb-Sb increases, which leads to the number of odd-numbered rings and make the crystallization speed slower.

4.2 Computational details

Al- and Ga-doped *a*-GST models are obtained via AIMD simulations by using the Vienna *Ab initio* Simulation Package (VASP). [53] The generalized-gradient approximation (GGA-PBE) parameterized by Perdew, Burke, and Ernzerhof is chosen for exchange-correlation functional. [18] For the projector augmented-wave (PAW) pseudopotentials [54], the valence electrons of $4s^2 4p^2$ for Ge, $5s^2 5p^3$ for Sb, $5s^2 5p^4$ for Te, $3s^2 3p^1$ for Al, $4s^2 4p^1$ for Ga, and $3d^{10} 4s^2$ for Zn are taken into considerations. The cutoff energy of 200 eV is set for cost-effective MD simulations and 400 eV for accurate structural relaxation. For the Brillouin-zone integration, a **k**-point of (0.25, 0.25, 0.25) is sampled during MD while the volume and shape of the cell and atomic coordinates are relaxed with $2 \times 2 \times 2$ Monkhorst-Pack grid.

The amorphous structures are obtained following the melt-quench method described in Ref. [110]. Initially, the structures are generated by randomly adding 144 atoms of GST with 0, 16 or 36 metal atoms into a cubic box, whose concentrations are corresponding to 0, 10, and 20 at.%, respectively. The size of the simulation box is determined to match the mass density to the theoretical value of undoped *a*-GST (5.6 g/cm^3 or 0.0296 atoms/Å^3), whose value is close to the experimental value of 0.0309 atoms/Å^3. [111, 112] In addition, the volume expansion by external doping is considered by setting the same mass density both for undoped and doped structures. In determining the composition of the doped GST, we assume that the composition of GST should be maintained to be 2:2:5 since the ratio of Ge:Sb:Te in Al-doped GST is kept to be 2:2:5. [82] The randomly positioned structures are premelted at 2000 K for 10 ps and equilibrated at 1000 K for 30 ps. Then, the liquid structure is quenched to 300 K with the rate of -15 K/ps. The time step for the MD simulation is chosen to 2 fs. Finally, the amorphous structures are fully relaxed with the cell shape and volume. The resulting equilibrium densities are 0.029, 0.030, and 0.029 atoms/Å^3 for undoped, Al-, and Ga-doped GST, respectively. The volume differences between the initial and final

structures are less than 5%. Five amorphous structures are independently generated for each case. We additionally generate two Al-doped GST models with 320 atoms to test the finite cell-size effects on structural properties, and the results of the bigger cells are equivalent to those of the smaller cells. For comparison, undoped a-GST is generated following the same method.

4.3 Structural properties

4.3.1 Local structures of Al- and Ga-doped amorphous GST

Structural information of the amorphous phase is generally represented by radial distribution function (RDF) which is a Fourier transform of the structure factor. For undoped and doped amorphous GST, total and partial RDFs are shown in Fig. 4.1 and in Fig. 4.2. For the total RDFs, the medium-range order beyond ∼4 Å does not change significantly with doping, positions of the first peak of doped amorphous GST are reduced regardless of kinds of the dopant. In Fig. 4.2, only Ge-Te bonds have little changes and others are largely changed by doping. To represent the detailed local environment, atom-resolved coordination number (CN) is also shown in Fig. 4.3.

As shown in Fig. 4.1, the first peaks of the doped a-GST are shifted inward with respect to that of the undoped amorphous GST. This is becuase the short metal-Te (M-Te) bonds are mainly formed by doping. The average M–Te lengths in Al- and Ga-doped a-GST represented by the position of the first peak in the partial radial distribution function, whose values are 2.66 and 2.69 Å, respectively. The present bond length of Ga–Te is in a good agreement with that in Ga–Sb–Te alloy (2.70 Å). [113] These are shorter than Ge–Te (2.79 Å) or Sb–Te (2.92 Å).

Figure 4.3 (a) shows that the dopants are mainly surrounded with Te atoms and the total CN of the dopants are close to four (heights of the hatched rectangle). The fourfold coordinated dopants in tetrahedral geometry show the peak of bond-angle distribution around dopants at 109.5°. These structural features are similar with those in the crystalline Al_2Te_3 ($P2_1/c$) and Ga_2Te_3 (Cc) where all metal atoms are surrounded with four Te atoms in a tetrahedral geometry. Such local environments are also observed in different chalcogenide systems (e.g. AlSbTe or GaSbTe alloy) [113, 114] where both Al and Ga atoms mainly bond with Te atoms and prefer the tetrahedral configuration. The robust preference for M-Te is attributed to the large difference in electronegativity, which can be confirmed by Bader charge analysis. The average

Bader charges for the elements are summarized in Table 4.1. Atoms bonded to the dopants show more negative charges than those in undoped a-GST, confirming that the dopants in a-GST act as cations. Bader charges of the dopants are close to those in the crystalline phase of Al_2Te_3 and Ga_2Te_3. We also note that the charges of the Ge, Sb, and Te atoms not bonded to the dopants are similar with those in undoped a-GST. In Fig. 4.3, Ga dopant prefers to Ge and Sb atoms more than Al dopant. This is because electronegativity of Al (1.61) is smaller than for Ga (1.81) and then ionic Ga is favorable in forming bonds with Ge or Sb more than Al. We find that the number of anionic Te–Te homopolar bonds is decreased (see Fig. 4.3 (d)) while dopant–dopant bonds are barely formed due to the strong M–Te bonds and the strong cationic feature of the dopant, respectivley.

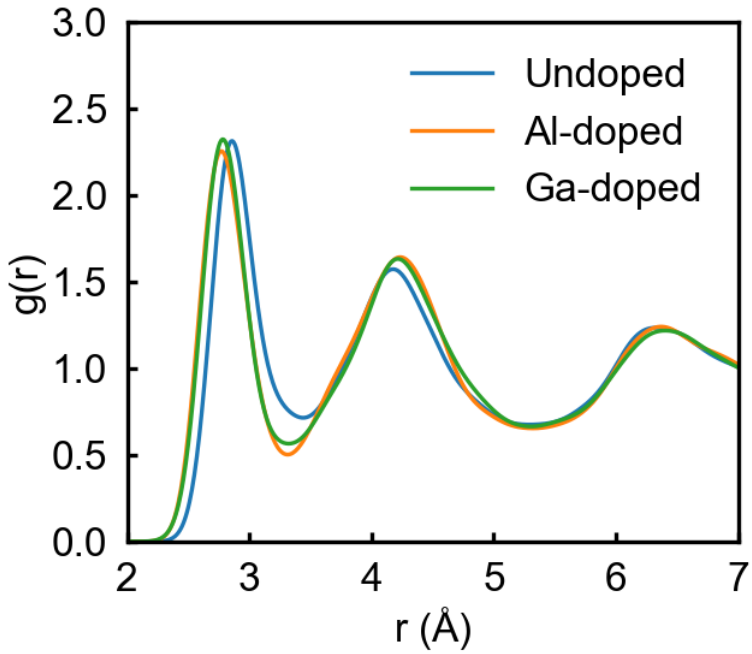

Fig. 4.1: Radial distribution functions of undoped and doped a-GST.

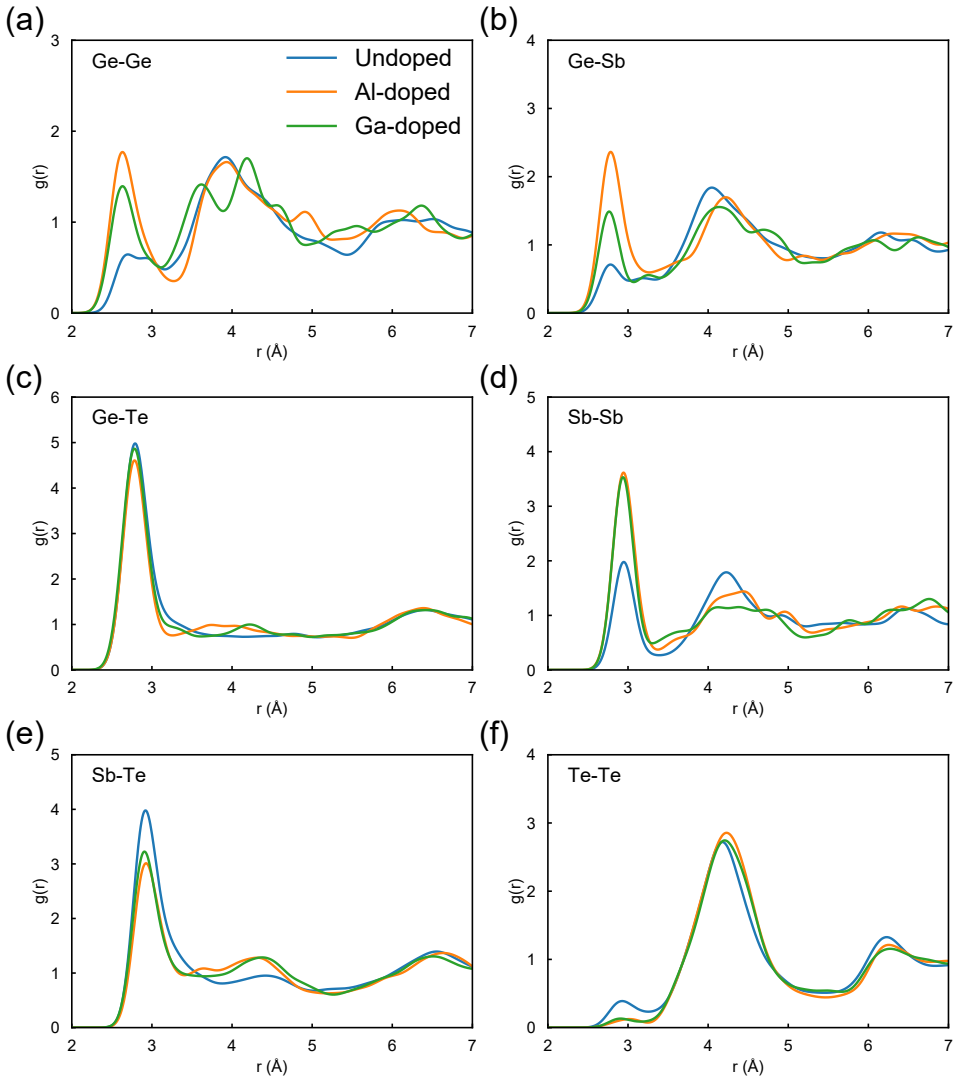

Fig. 4.2: Partial radial distribution functions of undoped and doped a-GST.

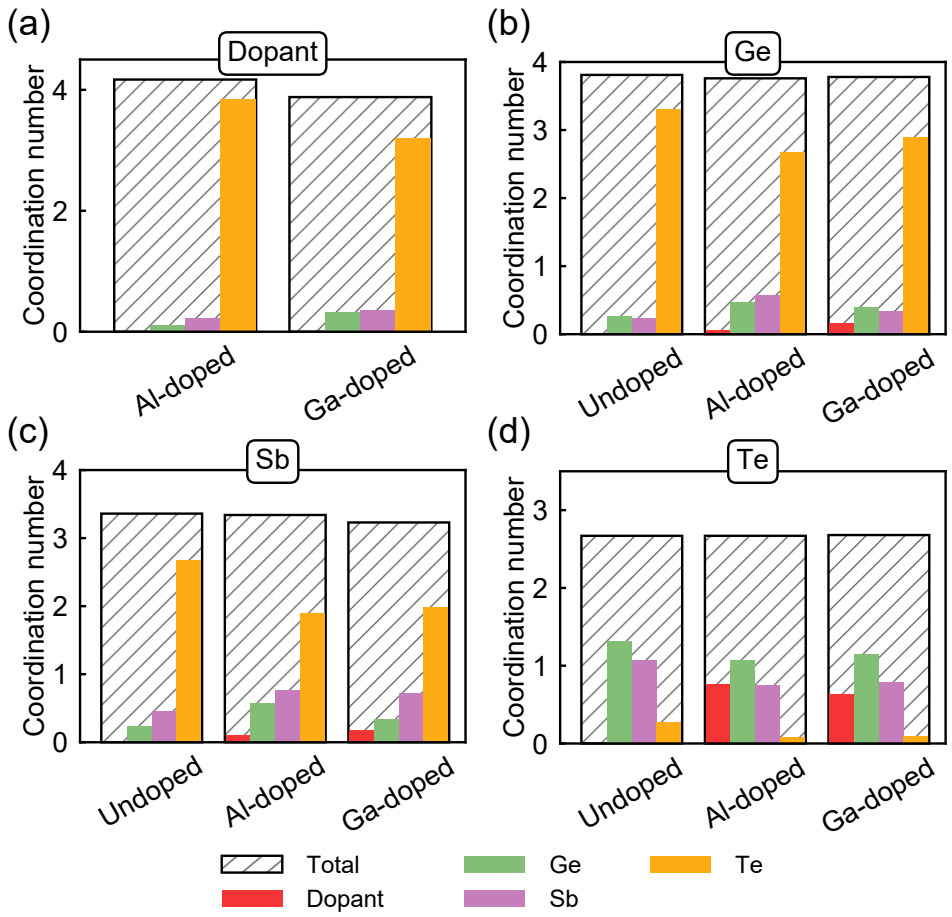

Fig. 4.3: Average coordination numbers around (a) dopant (b) Ge, (c) Sb, and (d) Te. The values is obtained by integrating the pair distribution functions of undoped and doped amorphous GST from 0 to 3.2 Å. The total coordination numbers are represented by hatched rectangles.

Table 4.1: Average Bader charges in the undoped, Al- and Ga-doped a-GST. "bo" means atoms bonded to dopants with a cutoff radius 3.2 Å, and "nb" other atoms. The values in parenthesis are Bader charges in the crystal structures. All the values are given in (positive) electronic charge.

	Undoped	Al-doped		Ga-doped	
		bo	nb	bo	nb
Ge	0.35	-0.14	0.31	0.16	0.33
Sb	0.41	-0.18	0.32	0.17	0.33
Te	-0.30	-0.72	-0.33	-0.36	-0.32
Dopant		1.73 (1.80)		0.49 (0.53)	

4.3.2 Ring statistics

For disordered systems, medium-range order structural features can be represented by ring structures. For the comparison, we check ring distributions in undoped and doped a-GST, which is shown in Fig. 4.4. The populations of the 3 and 4-fold rings are relatively similar with undoped a-GST, but the populations of the large size rings are increased by doping. As discussed in the previous section, the dopants mainly form bonds with Te atoms and the atom-resolved CNs of Te against Ge and Sb are decreased, which results in increasing of homopolar bonds such as Ge–Ge, Ge–Sb, and Sb–Sb. The average number of the homopolar bonds in the models are measured to 18.6 bonds/atoms in undoped GST,38.8 bonds/atoms in Al-doped GST, and 28.2 bonds/atoms in Ga-doped GST. In the large size rings, especially for odd-numbered rings, such homopolar bonds should be involved and then the ratio of ABAB-type (A = Ge or Sb, B = Te) rings to the total rings tend to decrease in doped a-GST.

The thermal stability of the amorphous phase can be indirectly evaluated by ring statistics. In particular, for GST, the fourfold rings are considered as the crystalline building blocks and clustered fourfold rings can act as nucleation sites. [43] Furthermore, the population of ABAB-type fourfold rings indicates the stability of the amorphous phase because the perfect crystal has the alternate arrangement in the rings. [71] Since crystallization involves the breaking of the homopolar bonds in the odd-numbered rings, the increased number of the odd-numbered rings in doped a-GST indicates that the stability of the amorphous phase is enhanced and the crystallization speed is retarded. For Al and Ga dopants, it was reported that the dopants enhance the thermal stability of the amorphous phase increasing the crystallization temperature. [82, 83, 100] The enhanced thermal stability by changes in the ring structures is consistent with the high crystallization temperature in the experiments.

In addition to ring distribtuions, we examine the planarity of the fourfold rings in undoped and doped a-GST. As shown in Fig. 4.5, Al and Ga doping have little effects on the local geometry of fourfold rings unlike the results of NNP for the pristine GeTe

(See Fig. 3.9). Since the number of the fourfold rings in the doped a-GST is a little smaller than undoped a-GST, the areas of the planarity distribution for the doped a-GST are relatively smaller than that for the undoped a-GST. However, there is no sign for overly flattened fourfold rings in the doped a-GST with respect to the undoped a-GST. Therefore, the similar interfacial energies between the crystalline and amorphous phases are expected for undoped and doped GST.

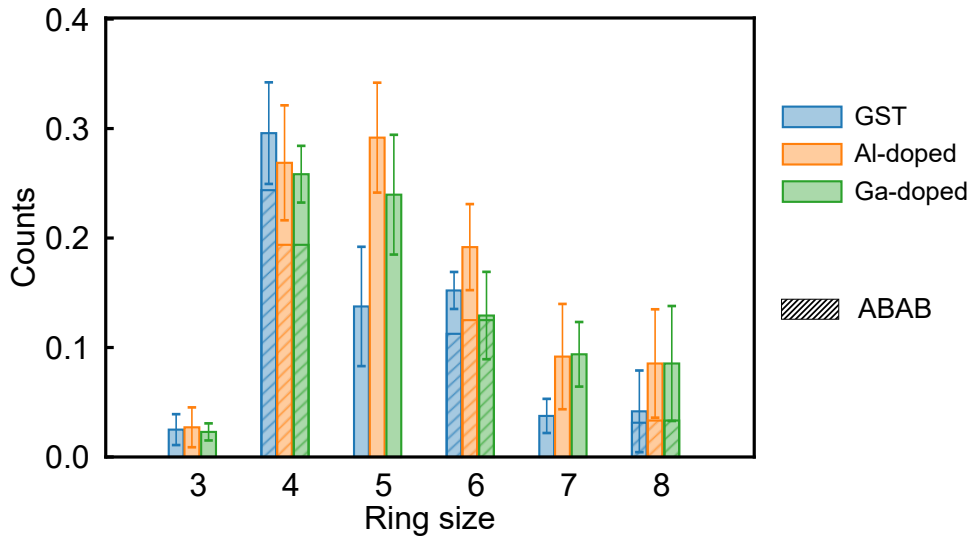

Fig. 4.4: Ring statistics for undoped and doped amorphous GST counted per atoms. All bonds within 3.2 Å are considered. The number of ABAB-type even-fold rings is shown in the hatched bar (A = Ge, Sb, and dopant, B = Te).

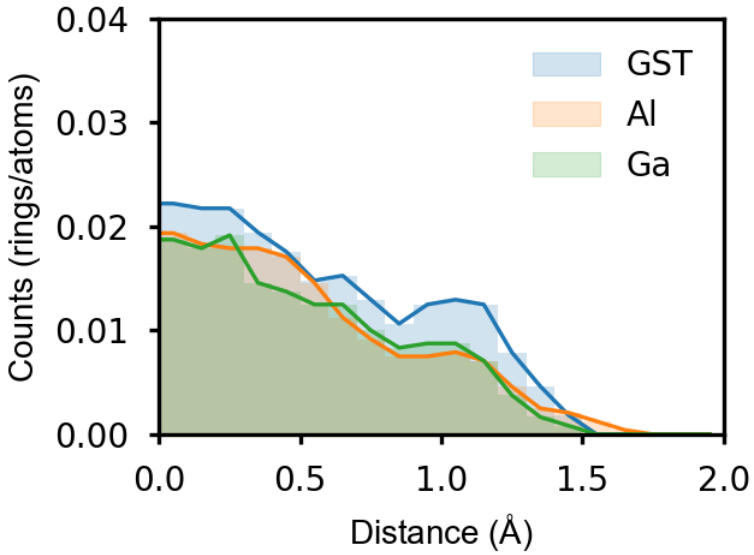

Fig. 4.5: Planarity of the fourfold rings in amorphous GST at 300 K. Bonds within 3.2 Å are considered.

4.3.3 Dopants in the crystalline phase

We evaluate the stable configuration for the dopants in the crystalline GST (c-GST) in terms of the defect formation energy. The dopants can occupy vacancy sites, interstitial sites, and substitutional sites for Ge, Sb, or Te. Since cation sites in c-GST are randomly occupied with Ge, Sb, and vacancies, the total energy of c-GST have a small range. Then, we examine the stable sites using five different crystalline models consisting of 72 atoms. Also, three different sites for each type of defects are evaluated and only those with the lowest energies are considered. For simple comparison, we consider only neutral charge state. The formation energy (E_f) is calculated by

$$E_f = E_{doped} - E_{undoped} + \sum_i (n_i \mu_i) \tag{4.1}$$

where E_{doped} and $E_{undoped}$ are the total energies of doped and undoped GST, and n_i and μ_i are the number of the added/removed element i and the chemical potential of the element i, respectively. By comparing the defect formation energies, we find that the octahedral vacancy sites are the most stable sites in the c-GST. Compared to the local environment in the amorphous state, the dopants are favorable in the octahedral geometry in the crystalline state. The difference in the stable configuration between the crystalline and amorphous state may require a larger activation energy and a transition time.

4.4 Dynamical properties

4.4.1 Diffusivity

The steady state nucleation rate and the growth velocity of a nucleus is dependent on dynamical properties. One representative physical quantity is diffusivity that is highly related to a kinetic factor. The diffusivity can be obtained from the slope of mean square displacement (MSD) with the following equation:

$$D = \frac{\langle r^* \rangle}{6t} \tag{4.2}$$

In order to investigate effects of doping on the kinetics of GST, the diffusivity is estimated at various temperatures (700, 800, 900, and 1000 K). Since the atomic motions is very slow at the temperatures near the glass transition temperature and too long time in AIMD scale is required to obtain sufficient MSD and accurate diffusivity, the high temperatures are set. Basically, the diffusivity is described by Arrhenius equation.

$$D = D_0 \exp\left(-\frac{E_d}{k_B T}\right) \tag{4.3}$$

where D_0 is a prefactor and E_d is an activation energy for diffusion. The data points and fitting lines are plotted in Fig. 4.6. The estimated values of E_d are 0.25, 0.25, and 0.29 eV for undoped, Al-doped, and Ga-doped GST, respectively.

It seems that the effects of Al on GST is different from those of Ga for dynamical property. In the case of Al doping, the activation energy for diffusion is close to the undoped GST, but the prefactor is decreased by half with respect to undoped GST. On the other hand, Ga doping increases the activation energy for diffusion. Although the diffusivities of undoped and Ga-doped GST are similar at 1000 K, the kinetics of Ga-doped GST slows down near the glass transition temperature. Both dopants retard the crystallization speed.

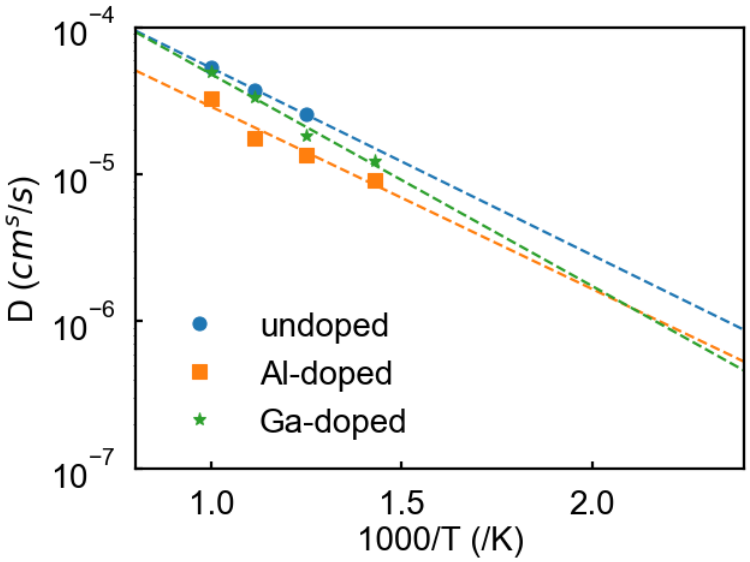

Fig. 4.6: Diffusivity of undoped and doped amorphous GST.

4.4.2 Interface-growth simulation

Homogeneous crystallization simulation for the phase change materials are usually carried out. In the case of GST consisting of a hundred atoms, the crystallization simulation is complete within a few hundreds picoseconds. Therefore, we also performed the homogeneous crystallization simulations for undoped and doped a-GST. However, the crystallization of Al- and Ga-doped GST were not finished over 500 ps at 600 K while the undoped GST is crystallized within ~ 300 ps. Since the length of the nucleation period cannot be estimated due to the stochastic nature, we employ an alternative way to validate the effects of the dopants on crystallization. Therefore, Crystalline growth is simulated from the crystalline template.

We replicate the one fcc structure by $3\times3\times4$ and three layers are frozen during MD. Other atoms move freely during the melt-quench process and crystallization simulation. The models at 0, 15, 30 ps are shown in Fig. 4.7. The green, blue, yellow, red, and pink balls represent Ge, Sb, Te, Al, and Ga, respectively. The three external dopants are involved in the models and positioned at one side of the crystalline template to compare the grwoth speed. During crysatallization, the dopants move slower than other atoms because MTe_4 units have the strong ionic character. This is consistent with low diffusivity of doped GST at high temperatures. Therefore, the crystalline parts grow fast from the opposit side of the template. After crystallization is complete, the dopants occupy the octahedral site in fcc lattice, which is in good agreement with the defect calculations.

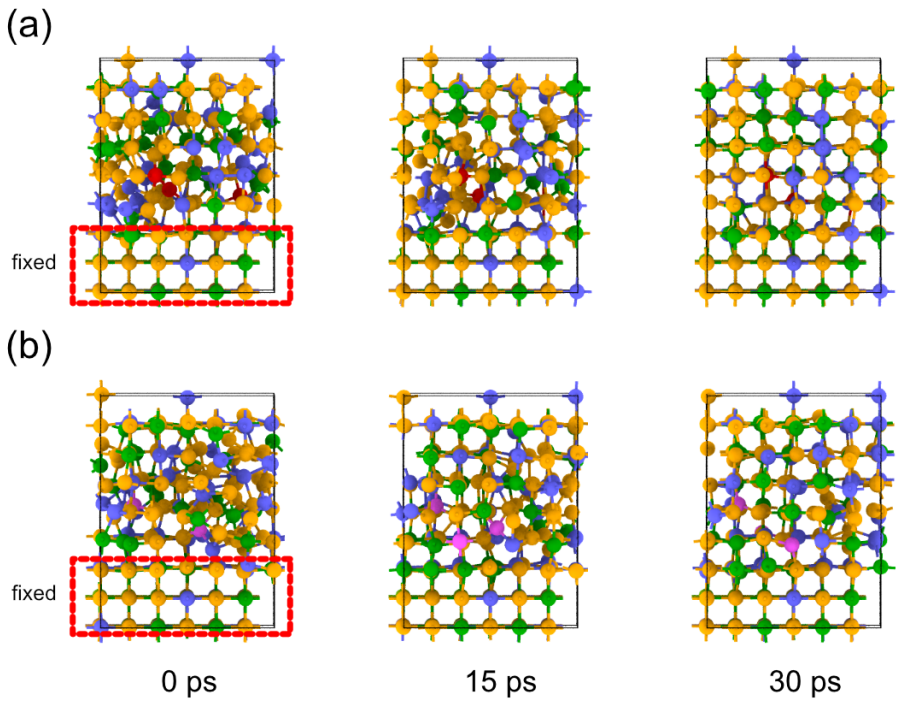

Fig. 4.7: Interface-growth simulations for (a) Al- and (b) Ga-doped GST. Three layers of fcc GST are fixed in the red box and others move without constraints during MD at 600 K. The green, blue, yellow, red, and pink balls represent Ge, Sb, Te, Al, and Ga, respectively.

4.5 Summary

We generated Al- and Ga-doped amorphous GST using AIMD and analyzed the effects of the dopants on the structural and dynamical properties. As strong cationic character of Al and Ga, the dopants form lots of bonds with Te atoms. This induces the increase of the homopolar bonds like Ge–Ge, Ge–Sb, and Sb–Sb. Although the planarity of the fourfold rings is not significantly affected by doping, the number of the odd-numbered rings is increased. Since the homopolar bonds in the odd-numbered rings should be broken, doping can hinder the crystallization of amorphous GST resulting in the higher stability of the amorphous phase. Besides, diffusivity in a-GST is retarded by doping, which reduces the growth speed.

Chapter 5

Conclusion

In this dissertation, we focus on finding key structural features that play a crucial role in the crystallization behaviors of the phase change materials. First, we developed NNP for GeTe to go beyond the scale limitations of DFT and performed the MD simulations to generate and crystallize the large-scale amorphous structure. In the developing stage, we validated the reliability of the NNP by comparing the structural properties of crystalline, liquid, and amorphous GeTe with the DFT results. We found that medium-range order in amorphous GeTe is crucial for crystallization. Although the size distribution of rings in the amorphous phase contributes to crystallization, the planarity of the fourfold rings in the amorphous phase is also correlated. As the planar fourfold rings is predominant, the interfacial energy between crystalline and amorphous phases is decreased, which makes the formation of a supercritical crystalline seed easy. Using the NNP, we acheived the realistic crystallization simulations using 4096-atom cell under the device condition. In particular, the incubation times are apparently observed during the simulations where it takes 7 or 17 ns for nulceation at 500 K. We can propose a microscopic model to deepen understanding of the crystallization ambiguous in the previous theoretical studies due to finite size effects and a short time scale. In addition to the pristine phase change material, we investigated the Al- and Ga-doped GST using DFT. The dopants act as strong cations and consume lots of Te atoms,

resulting in an increase of the homopolar bonds in amorphous GST. Then, the number of odd-numbered rings is increased. Unlike the pristine GeTe, Al and Ga doping change the size distribution of rings. Since the homopolar bonds in the odd-numbered rings should be broken and even-numbered rings should be formed upon the crystallization, the increased odd-numbered rings suppress the crystallization kinetics of amorphous GST. The studies of the pristine GeTe and doped GST help to understand the relation between the structural properties and crystallization kinetics. The medium-range order structures in the amorphous phase change materials significantly affect the nucleation stage. Based on this, we can suggest two desired strategies to accelerate the crystallization speed, especially for nucleation. One is that a pressured condition makes the planar fourfold ring favorable resulting in lowering the nucleation barrier. The other is that a dopant with a small electronegativity difference between Ge, Sb, and Te should be chosen. A large difference of electronegativity can make diffusivity slow and atomic rearrangement difficult, which leads to hindering crystallization. We expect that the findings help to design and explore new phase change materials and tune the properties of the phase change materials.

Bibliography

[1] V. Weidenhof, I. Friedrich, S. Ziegler, and M. Wuttig, Journal of Applied Physics **89**, 3168 (2001).

[2] A. V. Kolobov, P. Fons, A. I. Frenkel, A. L. Ankudinov, J. Tominaga, and Tomoya Uruga, Nature Materials **3**, 703 (2004).

[3] T. Kato and K. Tanaka, Japanese Journal of Applied Physics **44**, 7340 (2005).

[4] A. Chen, Solid-State Electronics **125**, 25 (2016).

[5] J. Hegedüs and S.R. Elliott, Nature Materials **7**, 399 (2008).

[6] J. M. Skelton, A. R. Pallipurath, T.-H. Lee, and S. R. Elliott, Advanced Functional Materials **24**, 7291 (2014).

[7] T. H. Lee, D. Loke, and S. R. Elliott, Advanced Materials **27**, 5477 (2015).

[8] M. L. Gallo and A. Sebastian, Journal of Physics D: Applied Physics **53**, 213002 (2020).

[9] L. Verlet, Physical Review **159**, 98 (1967).

[10] S. Nosé, The Journal of Chemical Physics **81**, 511 (1984).

[11] W. G. Hoover, Physical Review A **31**, 1695 (1985).

[12] M. Born and R. Oppenheimer, Annalen der Physik **457**, 389 (1927).

[13] P. Hohenberg and W. Kohn, Physical Review **136**, B864 (1964).

[14] W. Kohn and L. J. Sham, Physical review **140**, A1133 (1965).

[15] J. P. Perdew and W. Yue, Physical Review B **33**, 8800 (1986).

[16] A. D. Becke, Physical Review A **38**, 3098 (1988).

[17] J. P. Perdew, K. Burke, and M. Ernzerhof, Physical Review Letters **77**, 3865 (1996).

[18] J. P. Perdew, K. Burke, and M. Ernzerhof, Physical Review Letters **78**, 1396 (1997).

[19] J. P. Perdew, J. A. Chevary, S. H. Vosko, K. A. Jackson, M. R. Pederson, D. J. Singh, and C. Fiolhis, Physical Review B **46**, 6671 (1992).

[20] J. Behler and M. Parrinello, Physical Review Letters **98**, 146401 (2007).

[21] M. Gastegger, L. Schwiedrzik, M. Bittermann, F. Berzsenyi, and P. Marquetand, The Journal of Chemical Physics **148**, 241709 (2018).

[22] J. S. Smith, O. Isayev, and A. E. Roitberg, Chemical Science **8**, 3192 (2017).

[23] N. Srivastava, G. Hinton, A. Krizhevsky, I. Sutskever, and R. Salakhutdinov, Journal of Machine Learning Research **15**, 1929 (2014).

[24] J. Behler, International Journal of Quantum Chemistry **115**, 1032 (2015).

[25] D. Turnbull, Journal of Applied Physics **21**, 1022 (1950).

[26] C. V. Thompson and F. Spaepen, Acta Metallurgica **27**, 1855 (1979).

[27] F. Spaepen and R. B. Meyer, Scripta Metallurgica **10**, 257 (1976).

[28] I. Ronneberger, W. Zhang, and R. Mazzarello, MRS Communications **8**, 1018 (2018).

[29] J. Behler, Angewandte Chemie International Edition **56**, 12828 (2017).

[30] J. Behler, Physical Chemistry Chemical Physics **13**, 17930 (2011).

[31] A. P. Bartók, M. C. Payne, R. Kondor, and G. Csányi, Physical Review Letters **104**, 136403 (2010).

[32] G.C. Sosso, G. Miceli, S. Caravati, J. Behler, M. Bernasconi, Physical Review B **85**, 174103 (2012).

[33] G.C. Sosso, G. Miceli, S. Caravati, F. Giberti, J. Behler, M. Bernasconi, The Journal of Physical Chemistry Letters **4**, 4241 (2013).

[34] G.C. Sosso, M. Salvalaglio, J. Behler, M. Bernasconi, M. Parrinello, The Journal of Physical Chemistry C **119**, 6428 (2015).

[35] G.C. Sosso, J. Behler, M. Bernasconi, Physica Status Solid (b) **249**, 1880 (2012).

[36] G.C. Sosso, J. Colombo, J. Behler, E. Del Gado, M. Bernasconi, The Journal of Physical Chemistry B **118**, 13621 (2014).

[37] S. Gabardi, E. Baldi, E. Bosoni, D. Campi, S. Caravati, G.C. Sosso, J. Behler, M. Bernasconi, The Journal of Physical Chemistry C **121**, 23827 (2017).

[38] S. Gabardi, G.G. Sosso, J. Behler, M. Bernasconi, Faraday Discussions **213**, 290 (2019).

[39] T.H. Lee and S.R. Elliott, Physical Review Letters **107**, 145702 (2011).

[40] J. Akola and R. O. Jones, Physical Review B **76**, 235201 (2007).

[41] J. Kalikka, J. Akola, and R.O. Jones, Physical Review B **94**, 134105 (2016).

[42] J.Im, E. Cho, D. Kim, H. Horii, J. Ihm, and S. Han, Physical Review B **81**, 245211 (2010).

[43] K. Shinji, K. Kenichi, K. Shigeru, T. Hitoshi, U. Takeshi, S. Kentaro, T. Hiroshi, M. Yutaka, M. Toshiyuki, Y. Noboru, T. Yoshihito, S. Hiroyoshi, and T. Masaki, Applied Physics Letters **89**, 201910 (2006).

[44] D. Loke, T.H. Lee, W.J. Wang, L.P. Shi, R. Zhao, Y.C. Yeo, T.C. Chong, and S.R. Elliott, Science **336**, 1566 (2012).

[45] J. Kalikka, J. Akola, J. Larrucea, and R.O. Jones, Physical Review B **86**, 144113 (2012).

[46] M. Chen, K.A. Rubin, and R.W. Barton, Applied Physics Letters **49**, 502 (1986).

[47] S. Raoux, H.Y. Cheng, M.A. Caldwell, and H.S.P. Wong, Applied Physics Letters **95**, 071910 (2009).

[48] F. Xiong, A.D. Liao, D. Estrada, and E. Pop, Science **332**, 568 (2011).

[49] Y. Zhu, Z. Zhang, S. Song, H. Xie, Z. Song, X. Li, L. Shen, L. Li, L. Wu, and B. Liu, Materials Research Bulletin **64**, 333 (2015).

[50] S. Song, D. Yao, Z. Song, L. Gao, Z. Zhang, L. Li, L. Shen, L. Wu, B. Liu, Y. Cheng, and S. Feng, Nanoscale Research Letters **10**, 89 (2015).

[51] Y. Chen, G. Wang, L. Song, X. Shen, J. Wang, J. Huo, R. Wang, T. Xu, S. Dai, and Q. Nie, Crystal Growth & Design **17**, 3687 (2017).

[52] G. Bruns, P. Merkelbach, C. Schlockermann, M. Salinga, M. Wuttig, T.D. Happ, J.B. Philipp, and M. Kund, Applied Physics Letters **95**, 043108 (2009).

[53] G. Kresse and J. Hafner, Physical Review B **47**, 558 (1993).

[54] P. E. Blöchl, Physical Review B **50**, 17953 (1994).

[55] D. Yoo, K. Lee, W. Jeong, D. Lee, S. Watanabe, and S. Han, Physical Review Materials **3**, 093802 (2019).

[56] K. Lee, D. Yoo, W. Jeong, and S. Han, Computer Physics Communications **242**, 95 (2019).

[57] J. Behler, The Journal of Chemical Physics **134**, 074106 (2011).

[58] N. Artrith and A. Urban, Computational Materials Science **114**, 135 (2016).

[59] A. Velea, F. Sava, G. Socol, A.M. Vlaicu, C. Mihai, A. Lörinczi, and I.D. Simandan, Journal of Non-Crystalline Solids **492**, 11 (2018).

[60] J.P. McHuglz and W.A. Tiller, Transactions of the Metallurgical Society of AIME. **218**, 187 (1960).

[61] S. Le Roux and P. Jund, Computational Materials Science **49**, 70 (2010).

[62] R. Hashimoto, Y. Shibuta, and T. Suzuki, ISIJ International **51**, 1664 (2011).

[63] J. Orava and A.L. Greer, Acta Materialia **139**, 226 (2017).

[64] A. Sebastian, N. Papandreou, A. Pantazi, H. Pozidis, and E. Eleftheriou, Journal of Applied Physics **110**, 084505 (2011).

[65] A. Faraclas, F. Dirisaglik, and A. Gokirmak, IEEE Transactions on Electron Devices **61**, 372 (2014).

[66] A.V. Kolobv, J. Tominaga, P. Fons, and T. Uruga, Applied Physics Letters **82**, 382 (2003).

[67] X. Zhou, L. Wu, Z. Song, F. Rao, M. Zhu, C. Peng, D. Yao, S. Song, B. Liu, and S. Feng, Applied Physics Letters **101**, 142105 (2012).

[68] Q. Hubert, C. Jahan, V. Sousa, L. Perniola, A. Kusiak, J.-L. Battaglia, P. Noé, M. Bernard, C. Sabbione, M. Tessaire, F. Pierre, P. Zuliani, R. Annunziata, G. Pananakakis, and B. de Salvo, International Conference on Solid State Devices and Materials pp. Fukuoka, 24–27 September (2013).

[69] J. H. Park, S.-W. Kim, J. H. Kim, Z. Wu, S. L. Cho, D. Ahn, D. H. Ahn, J. M. Lee, S. U. Nam, and D.-H. Ko, Journal of Applied Physics **117**, 115703 (2015).

[70] W. Zhou, L. Wu, X. Zhou, F. Rao, Z. Song, D. Yao, W. Yin, S. Song, B. Liu, B. Qian, and S. Feng, Applied Physics Letters **105**, 243113 (2014).

[71] E. Cho, Y. Youn, and S. Han, Applied Physics Letters **99**, 183501 (2011).

[72] X. Zhou, M. Xia, F. Rao, L. Wu, X. Li, Z. Song, S. Feng, and H. Sun, ACS Applied Materials & Interfaces **6**, 14207 (2014).

[73] K. B. Borisenko, Y. Chen, D. J. H. Cockayne, S. A. Song, and H. S. Jeong, Acta Materialia **59**, 4335 (2011).

[74] Y. Kim, K. Jeong, M.-H. Cho, U. Hwang, H. S. Jeong, and K. Kim, Applied Physics Letters **90**, 171920 (2007).

[75] K.-H. Song, J.-H. Kim, J.-H. Seo, and H.-Y. Lee, Journal of Optoelectronics and Advanced Materials **11**, 1988 (2009).

[76] S. Privitera, E. Rimini, and R. Zonca, Applied Physics Letters **85**, 3044 (2004).

[77] S. Privitera, E. Rimini, C. Bongiorno, A. Pirovano, and R. Bez, Nuclear Instruments and Methods in Physics Research B **257**, 352 (2007).

[78] K. Kim, J.-C. Park, J.-G. Chung, S. A. Song, M.-C. Jung, Y. M. Lee, H.-J. Shin, B. Kuh, Y. Ha, and J.-S. Noh, Applied Physics Letters **89**, 243520 (2006).

[79] M.-C. Jung, Y. M. Lee, H.-D. Kim, M. G. Kim, H. J. Shin, K. H. Kim, S. A. Song, H. S. Jeong, C. H. Ko, and M. Han, Applied Physics Letters **91**, 083514 (2007).

[80] E. Cho, S. Han, D. Kim, H. Horii, and H.-S. Nam, Journal of Applied Physics **109**, 043705 (2011).

[81] M. H. Jang, S. J. Park, D. H. Lim, M.-H. Cho, K. H. Do, D.-H. Ko, and H. C. Sohn, Applied Physics Letters **95**, 012102 (2009).

[82] G. Wang, X. Shen, Q. Nie, R. Wang, L. Wu, Y. Lv, F. Chen, S. Dai, and J. Li,, Journal of Physics D: Applied Physics **45**, 375302 (2012).

[83] S. Wei, J. Li, X. Wu, P. Zhou, S. Wang, Y. Zheng, L. Chen, F. Gan, X. Zhang, and G. Li, Optics Express **15**, 10584 (2007).

[84] J.-H. Seo, K.-H. Song, and H.-Y. Lee, Journal of Applied Physics **108**, 064515 (2010).

[85] Y. Ling, Y. Lin, B. Qiao, Y. Lai, J. Feng, T. Tang, B. Cai, and B. Chen, Japanese Journal of Applied Physics **45**, L349 (2006).

[86] B. Qiao, J. Feng, Y. Lai, Y. Ling, Y. Lin, T. Tang, B. Cai, and B. Chen, Applied Surface Science **252**, 8404 (2006).

[87] J. Feng, Y. Zhang, B. W. Qiao, Y. F. Lai, Y. Y. Lin, B. C. Cai, T. A. Tang, and B. Chen, Applied Physics A **87**, 57 (2007).

[88] J. M. Skelton and S. R. Elliott, Journal of Physics: Condensed Matter **25**, 205801 (2013).

[89] T. Fukushima, H. Katayama-Yoshida, K. Sato, H. Fujii, E. Rabel, R. Zeller, P. H. Dederichs, W. Zhang, and R. Mazzarello, Physical Review B **90**, 144417 (2014).

[90] Y. Fukuma, N. Nishimura, F. Odawara, H. Asada, and T. Koyanagi, J. Supercond. Incorporating Nov. Magn. **16**, 71 (2003).

[91] Q. Wang, B. Liu, Y. Xia, Y. Zheng, R. Huo, Q. Zhang, S. Song, Y. Cheng, Z. Song, and S. Feng, Applied Physics Letters **107**, 222101 (2015).

[92] W. Zhang, I. Ronneberger, Y. Li, and R. Mazzarello, Advanced Materials **24**, 4387 (2012).

[93] Y. Fukuma, H. Asada, M. Arifuku, and T. Koyanagi, Applied Physics Letters **80**, 1013 (2002).

[94] H. Shingai, T. Kato, M. Kosuda, Y. Takagi, H. Oyake, and H. Hirata, Japanese Journal of Applied Physics **49**, 08KG02 (2010).

[95] J. M. Skelton, T. H. Lee, and S. R. Elliott, Applied Physics Letters **101**, 024106 (2012).

[96] W.-D. Song, L.-P. Shi, X.-S. Miao, and C.-T. Chong, Advanced Materials **20**, 2394 (2008).

[97] Y. Li and R. Mazzarello, Advanced Materials **24**, 1429 (2012).

[98] R. Li, Y. Jiang, L. Xu, Z. Ma, F. Yang, J. Xu, and W. Su, Phys. Status Solidi A **210**, 2650 (2013).

[99] G. Wang, Q. Nie, X. Shen, R. P. Wang, L. Wu, J. Fu, T. Xu, and S. Dai, Applied Physics Letters **101**, 051906 (2012).

[100] Y. Lu, Z. Zhang, S. Song, X. Shen, G. Wang, L. Cheng, S. Dai, and Z. Song, Applied Physics Letters **102**, 241907 (2013).

[101] D. H. Kim, M. S. Kim, R.-Y. Kim, K. S. Kim, and H. G. Kim, Materials Characterization **58**, 479 (2007).

[102] K.-H. Song, S.-W. Kim, J.-H. Seo, and H.-Y. Lee, Journal of Applied Physics **104**, 103516 (2008).

[103] K.-H. Song, S.-W. Kim, J.-H. Seo, and H.-Y. Lee, Thin Solid Films **517**, 3958 (2009).

[104] B. Prasai, G. Chen, and D. A. Drabold, Applied Physics Letters **102**, 041907 (2013).

[105] K. Wang, C. Steimer, D. Wamwangi, S. Ziegler, and M. Wuttig, Applied Physics A **80**, 1611 (2005).

[106] K. Wang, C. Steimer, D. Wamwangi, S. Ziegler, M. Wuttig, J. Tomforde, and W. Bensch, Microsystem Technologies **13**, 203 (2007).

[107] W. D. Song, L. P. Shi, X. S. Miao, and T. C. Chong, Applied Physics Letters **90**, 091904 (2007).

[108] T.-J. Park, S.-Y. Choi, and M.-J. Kang, Thin Solid Films **515**, 5049 (2007).

[109] K. Wang, D. Wamwangi, S. Ziegler, C. Steimer, and M. Wuttig, Journal of Applied Physics **96**, 5557 (2004).

[110] E. Cho, J. Im, C. Park, W. J. Son, D. H. Kim, H. Horii, J. Ihm, and S Han, Journal of Physics: Condensed Matter **22**, 205504 (2010).

[111] E. Cho, J. Im, C. Park, W. J. Son, D. H. Kim, H. Horii, J. Ihm, and S. Han,, J. Phys. Condes. Matter **22**, 205504 (2010).

[112] W. K. Njoroge, H.-W. Wöltgens, and M. Wuttig, J. Vac. Sci.Technol. A **20**, 230 (2002).

[113] A. Bouzid, S. Garbardi, C. Massobrio, M. Boero, and M. Bernasconi, Physical Review B **91**, 184201 (2015).

[114] M. Xia, K. Ding, F. Rao, X. Li, L. Wu, and Z. Song, Scientific Reports **5**, 8548 (2015).

초 록

상변화 메모리는 차세대 비휘발성 메모리 기술로 유망한 기술이다. 새로운 메모리 기술들 중에서 상변화 메모리는 이미 성공적으로 상용화될 정도로 성숙한 기술이다. 하지만, 여전히 원자수준의 상전이 거동에 대한 기초적인 이해가 부족하다. 분자동역학을 이용하여 상변화 물질의 상전이 과정을 효과적으로 이해할 수 있기 때문에, 결정화 시뮬레이션을 진행하였고 비정질의 중거리 차수 구조가 결정화 과정에 미치는 영향에 대해 살펴보았다.

먼저, 대표적인 상변화 물질인 GeTe에 대하여 인공신경망 퍼텐셜을 개발하였고, 이를 이용하여 비정질 GeTe의 결정화에 대해 연구하였다. 밀도 범함수 이론의 정확도와 값싼 계산 비용으로 소자에서 일어나는 상전이 조건에 가깝게 모델링할 수가 있었다. 이 퍼텐셜을 개발하는 과정에서 비정질 구조의 사각형 링 구조의 입체적 형태가 결정화의 핵생성 과정에 중대한 영향을 주는 것을 확인하였다. 이차원에 가까운 사각형 링이 비정질 상에서 많이 존재할수록 핵생성 과정이 잘 일어나는 것을 보았다. 구부려진 사각형 링 구조를 포함와 같은 입체적인 링 구조들을 포함한 비정질 구조를 학습 데이터에 추가함으로써 밀도 범함수 이론의 결과에 가까운 비정질 구조를 얻을 수 있었다. 이러한 구조적인 개선이 비정질과 결정질의 계면 에너지를 높여주었다. 개선된 인공신경망 퍼텐셜을 이용하여 결정화 시뮬레이션을 두 가지 밀도와 네 가지 온도 조건에서 수행하였다. 모든 결정화 과정에서 핵생성에 걸리는 유효한 시간이 존재하는 것을 확인하였고, 특히 소자 내부의 평형 밀도를 고려한 경우 실험에서 보고되는 30 ns에 유사한 정도로 7과 17 ns의 시간이 핵생성에 소요되는 것을 확인하였다.

실질적으로 소자에서는 Ge-Sb-Te 화합물에 도핑을 하여 물성을 조절하는 경우가 많다. 그러나 이런 다성분계의 경우까지 인공신경망 퍼텐셜을 개발하는 데는 현재 수준으로는 과도한 계산 비용을 소모하게 된다. 따라서, Al과 Ga 도핑된 GST에 대해서는 제일원리 계산을 통해서 도핑 효과에 대해 연구하였다. Al과 Ga은 비정질 GST에서 네 개의 Te에 사면체 형태로 둘러 쌓인 구조를 많이 갖게 되며 양이온적

성질을 보여주었다. 이는 GST에서 Ge-Ge, Ge-Sb, Sb-Sb와 같은 동종결합 수를 증가시켰고, 홀수 개의 링 구조가 증가하게 되었다. 결정화가 되기 위해서는 짝수 개의 링 구조로 변화해야 하기 때문에 이러한 홀수 링의 증가는 결정화를 어렵게 만들고 비정질 상의 안정성을 높이는 효과를 주는 것을 예상할 수 있다.

주요어: 상변화 물질, 인공신경망 퍼텐셜, 결정화 거동
학번: 2014-21434